

Attention-based Neural Network Emulators for Multi-Probe Data Vectors Part I: Forecasting the Growth-Geometry split

Kunhao Zhong,^{1,2*} Evan Saraivanov¹, James Caputi¹, Vivian Miranda³, Supranta S. Boruah⁴, Tim Eifler⁴, Elisabeth Krause^{4,5}

¹*Department of Physics and Astronomy, Stony Brook University, Stony Brook, NY 11794, USA*

²*Department of Physics and Astronomy, University of Pennsylvania, Philadelphia, PA 19104, USA*

³*C. N. Yang Institute for Theoretical Physics, Stony Brook University, Stony Brook, NY 11794, USA*

⁴*Department of Astronomy and Steward Observatory, University of Arizona, 933 N Cherry Ave, Tucson, AZ 85719, USA*

⁵*Department of Physics, University of Arizona, 1118 E Fourth Str, Tucson, AZ, 85721-0065, USA*

Accepted XXX. Received YYY; in original form ZZZ

ABSTRACT

We present a new class of machine-learning emulators that accurately model the cosmic shear, galaxy-galaxy lensing, and galaxy clustering real space correlation functions in the context of Rubin Observatory year one simulated data. To illustrate its capabilities in forecasting models beyond the standard Λ CDM, we forecast how well LSST Year 1 data will be able to probe the consistency between geometry Ω_m^{geo} and growth Ω_m^{growth} dark matter densities in the so-called split Λ CDM parameterization. When trained with a few million samples, our emulator shows uniform accuracy across a wide range in an 18-dimensional parameter space. We provide a detailed comparison of three neural network designs, illustrating the importance of adopting state-of-the-art Transformer blocks. Our study also details their performance when computing Bayesian evidence for cosmic shear on three fiducial cosmologies. The transformers-based emulator is always accurate within POLYCHORD’s precision. As an application, we use our emulator to study the degeneracies between dark energy models and growth geometry split parameterizations. We find that the growth-geometry split remains to be a meaningful test of the smooth dark energy assumption.

1 INTRODUCTION

Markov Chain Monte Carlo (MCMC) is a common and effective technique for inferring cosmological parameters, as it enables the exploration of high-dimensional likelihoods from a wide range of data sets. These include space and ground-based measurements of the Cosmic Microwave Background (CMB) (Planck Collaboration et al. 2020a; Aiola et al. 2020; Dutcher et al. 2021), type Ia supernova (Scolnic et al. 2018, 2022), Baryon Acoustic Oscillations (BAO) (Ross et al. 2015; Alam et al. 2017; Raichoor et al. 2020; Alam et al. 2021; Zhao et al. 2022), and lensing and clustering of optical galaxies (Hikage et al. 2019; Hamana et al. 2020; Nicola et al. 2020; Asgari et al. 2021; Heymans et al. 2021; Abbott et al. 2022).

Forthcoming stage-IV surveys will observe the lensing and clustering of optical galaxies with unparalleled precision. These experiments include the Dark Energy Spectroscopic Instrument (DESI Collaboration et al. 2023), the Large Synoptic Survey Telescope (LSST) (Ivezić et al. 2019), the Euclid mission (Laureijs et al. 2011), and the Roman Space Telescope (Dore et al. 2019). They all aim to provide a more ambitious investigation into the nature of dark energy and dark matter, with a corresponding increase in the model complexity of nuisance physics. For example, new analyses will consider parameterizations for galaxy biases and intrinsic alignments that are better-motivated from an effective field theory perspective (Kokron et al. 2021; Mergulhão et al. 2022; Bakx et al. 2023; Chen & Kokron 2023; Nicola et al. 2023; Rubira & Schmidt 2023). The dark sector may simultaneously include new physics in the early (Carrillo González et al. 2021; Benevento et al. 2022; Hill et al. 2022; Buen-Abad et al. 2023; Berryman et al. 2023; Franco Abellán et al. 2023; McDonough et al. 2023; Niedermann & Sloth 2023;

Poulin et al. 2023; Ramadan et al. 2023), intermediate (Simon et al. 2022; Holm et al. 2022; Alvi et al. 2022; Anchordoqui et al. 2022; Ashoorioon & Davari 2023; Bucko et al. 2023; Holm et al. 2023; Nygaard et al. 2023; Rubira et al. 2023), and late Universes (Gleyzes et al. 2015; Zumalacárregui et al. 2017; Nesseris et al. 2017; Peirone et al. 2018; Espejo et al. 2019; Sakr & Martinelli 2022; Amon & Efstathiou 2022; Berghaus et al. 2023; Lin et al. 2023; Wang et al. 2023; Zhong et al. 2023), as simple alternatives to Λ CDM is shown to be ineffective in explaining current tensions (Schöneberg et al. 2022).

Future investigations into the dark sector and nuisance physics are expected to have higher dimensionality of the parameter space and larger execution time per model. For example, CMB constraints from the damping tail of the temperature power spectrum at multipoles $\ell \gtrsim 3000$ will soon require additional parameters related to baryonic physics (McCarthy et al. 2022). The stiff increase in computational costs associated with running MCMC simulations is inevitable as the precision of theory predictions must align with the reduced uncertainties of new experiments.

Indeed, the current computational costs associated with evaluating some statistical metrics that assess tension and goodness-of-fit are already slowing the research progress. Currently, MCMCs aimed at constraining early dark energy scenarios, often employing a combination of CMB data measured by Planck and ACT experiments (Hill et al. 2022), can take weeks to satisfy the stringent $R - 1 \approx 0.005$ Gelman-Rubin convergence threshold (Gelman & Rubin 1992). This criterion is necessary for robustly assessing goodness-of-fit (Raveri & Hu 2019). Moreover, the marginalization of Early Dark Energy predictions over general late-time dark energy equations of state further

increases the computational demands of MCMCs, with convergence being achieved only after months of continuous runs (Rebouças et al. 2023). As the standard Λ CDM model undergoes simultaneous generalizations in the early and late times to potentially solve multiple existing tensions (or to stress test the standard model), these demanding analyses are expected to become more common.

Forecasts of the upcoming Simons Observatory, CMB-S4, and CMB-HD experiments have shown the need for enhancements in the accuracy settings of CLASS (Blas et al. 2011) and CAMB (Lewis & Bridle 2002; Howlett et al. 2012) Boltzmann codes. These new settings considerably increase the run time per model, even when predictions are restricted to the Λ CDM model (McCarthy et al. 2022; MacInnis et al. 2023). Exploring the viability of new theories with Bayesian tools may soon become impractical even when abundant computational resources are available, especially considering that interpreting tension metrics requires calibration with simulated data (Miranda et al. 2021).

A promising strategy to address these challenges lies in the development of accurate machine learning-based emulators for the theoretical data vectors; they have proven beneficial in a myriad of forecasts (Manrique-Yus & Sellentin 2020; Spurio Mancini et al. 2022; Günther et al. 2022; Boruah et al. 2023; To et al. 2023). The training and validation of emulators involve calculating tens of thousands, sometimes millions, of data vectors. However, training is cost-effective compared to MCMCs since the evaluations can be trivially parallelized. There is also no need for the emulator to be able to extrapolate its predictions to regions in parameter space outside the boundary of training, which simplifies the underlying machine learning architecture and reduces the training time.

Emulators based on the simpler multilayer perceptron machine learning design can accurately predict CMB and weak lensing data vectors in Fourier space over large volumes in parameter space (Spurio Mancini et al. 2022). In recent studies, Boruah et al. (2023) and To et al. (2023) successfully created emulators that compute the real-space cosmic shear, galaxy-galaxy lensing, and galaxy clustering two-point correlation functions of current- and next-generation of optical surveys based on widely adopted deep learning designs. In both cases, the complexity of data vectors in real space restricted the volume of parameter space in which these emulators could provide meaningful results.

For instance, Boruah et al. (2023) trained the emulator using an adaptive method that is more or less equivalent to a temperate MCMC with a temperature of a few around an arbitrary cosmology (temperature is a scalar that broadens the covariance matrix). The resulting emulator fails to provide accurate results when the MCMC best-fit cosmology shifts more than a few sigmas away from the fiducial model assumed on training. This failing can happen whenever forecasting is performed around a different cosmology or in analysis with actual data if the high likelihood region is far from the fiducial training model. As long as their emulator is constantly retrained, and their training method is significantly cheaper than what we propose in this work, this limitation is not a significant problem, as both Boruah et al. (2023) and To et al. (2023) had the confined aim to create methods for approximate computing 68% and 95% confidence regions in MCMCs.

Nevertheless, there are instances where it is advantageous to have emulators with a large volume of applicability in parameter space. When dealing with actual data, the combination of likelihoods from various experiments can shift parameters noticeably; this requires constant emulator retraining whenever the data combination changes (and there are a lot of possible combinations). Another case involves the computation of the Bayesian evidence, which is more sensitive

to the modeling accuracy on the tails of the probability distribution. Various samplers are available to compute Bayesian evidence, including MULTINEST (Feroz & Hobson 2008), POLYCHORD (Handley et al. 2015), DYNesty (Speagle 2020), POCOmc (Karamanis et al. 2022), and NAUTILUS (Lange 2023). Each of them employs a different algorithm that contains hyperparameters that must be tuned to the target posterior distribution, necessitating calibration with synthetic data vectors that can be extremely expensive (Miranda et al. 2021; Lemos et al. 2023).

In this paper we study the growth geometry split, which is a phenomenological test that duplicates two parameters in w CDM cosmologies, the cold dark matter density Ω_m and the dark energy equation of state w (Wang et al. 2007; Ruiz & Huterer 2015b; Muir et al. 2021; Ruiz-Zapatero et al. 2021; Nguyen et al. 2023; Zhong et al. 2023). The additional parameters disentangle the background and growth factor behaviors; their consistency is a key prediction of the so-called smooth dark energy paradigm (Mortonson et al. 2009). Following Zhong et al. (2023), the parameters that only modify the growth factor are Ω_m^{growth} and w^{growth} . Finally, Λ CDM-split is the particular case where $w^{\text{geo}} = w^{\text{growth}} = -1$.

This paper is organized as follows. In Sec. 2, we present the assumptions for LSST-Y1 forecasting and the main steps for implementing our proposed emulator. In Sec. 3, we provide details of the emulator training and validation. As an application in an extension to Λ CDM, we provide LSST-Y1 forecasts for the so-called growth-geometry w CDM split in Sec. 4. Finally, we discuss the possible use of the emulator and compare it with previous work in Sec. 5.

2 METHODOLOGY

We detail in this paper the training and validation of machine-learning emulators that can simulate the real-space data vector of cosmic shear (ξ_+, ξ_-), galaxy-galaxy lensing (γ_t), galaxy clustering (w), and their combination (3x2pt) in the context of Rubin Observatory year one (LSST-Y1) (The LSST Dark Energy Science Collaboration et al. 2018). Our adopted cosmology is the growth-geometry w CDM split model (Wang et al. 2007; Ruiz & Huterer 2015a; Muir et al. 2021; Zhong et al. 2023), which we introduce in Sec. 4. Regarding the LSST-Y1 forecast choices, we closely follow the methodologies outlined in Boruah et al. (2023), which are themselves based on the DESC collaboration science requirement document (The LSST Dark Energy Science Collaboration et al. 2018). The first year's data from Rubin is expected to have an observed survey area of 12300 deg², with shape noise of $\sigma_e = 0.26$, and an effective number density of source galaxies $n_{\text{eff}} = 11.2 \text{ arcmin}^{-2}$.

The 3x2pt data vector has 1560 data points before scale-cuts, divided into five tomographic lens bins and five tomographic source bins with angular scales between 2.5 and 900 arcmin. In both the training and validation of our emulator, we included all data points without any prior scale cuts. However, we later apply the scale-cut $\theta_{\text{min}} = \{2.756, 8.696\}$ arcmin on the cosmic shear components $\{\xi_+, \xi_-\}$. We additionally applied angular scale cuts corresponding to the physical scale $R_{\text{min}} = 21h^{-1}$ Mpc when computing galaxy-galaxy lensing. We calculated the covariance matrix with CosmoCov (Fang et al. 2020; Krause & Eifler 2017), accounting for the Gaussian, connected non-Gaussian, and super-sample components.

The systematics modeling incorporates multiplicative shear calibration m_i , photometric redshift uncertainties with shifts $\Delta z_{i/s}^i$ (lens and source bins), intrinsic alignment (IA) via the non-linear alignment modeling (Bridle & King 2007), and linear galaxy bias b_i . These parameters are listed in Table 1. We compute the data vec-

Parameter	Fiducial Value	Prior
Standard Cosmology		
Ω_m^{geo}	0.3166	FLAT[0.24, 0.4]
Ω_b	0.0493	FLAT[0.04, 0.06]
$\ln(10^{10} A_s)$	3.045	FLAT[2.84, 3.21]
n_s	0.9649	FLAT[0.92, 1.0]
H_0	67.32	FLAT[61, 73]
w^{geo}	-1	FLAT[-1.3, -0.7]
τ	-	FLAT[0.01, 0.2]
Split Parameters		
Ω_m^{growth}	0.3166	FLAT[0.24, 0.4]
w^{growth}	-1	FLAT[-1.3, -0.7]
Linear Galaxy bias		
b_1	1.73	FLAT[0.8, 3.0]
b_2	1.65	FLAT[0.8, 3.0]
b_3	1.61	FLAT[0.8, 3.0]
b_4	1.93	FLAT[0.8, 3.0]
b_5	2.12	FLAT[0.8, 3.0]
Intrinsic Alignment		
a_1	0.5	FLAT[-5, 5]
η_1	0	FLAT[-5, 5]
Source photo-z		
$\Delta z_s^i \times 10^2$	0	GAUSS[0, 0.2]
Lens photo-z		
$\Delta z_l^i \times 10^2$	0	GAUSS[0, 0.2]
Shear calibration		
$m_i \times 10^2$	0	GAUSS[0, 0.5]

Table 1. Prior distributions and fiducial values for the cosmological and nuisance parameters utilized in our LSST-Y1 forecasts. The priors conform to either the uniform distribution, displayed as FLAT[MIN, MAX], or the normal distribution, displayed as GAUSS[MEAN, STANDARD DEVIATION]. When training the emulators, we set the bounds of the Latin Hypercube and uniform samplings that distributed the parameters to the limits of the flat priors except for τ . We did not expand the training edges to avoid degradation of the emulator performance near the boundaries. We also set hard edges on parameters that obey the normal distribution to $[-3.3 \times \text{standard deviation}, +3.3 \times \text{standard deviation}]$ when training the emulator. However, when running the chains, we did not apply these additional cuts.

tors using the COSMOLIKE software (Eifler et al. 2014; Krause & Eifler 2017), and manage the MCMC chains using the COBAYA sampler (Torrado & Lewis 2021). Both packages are integrated in the COBAYA-COSMOLIKE Architecture, or CoCoA¹.

2.1 Emulator Design and Training

The baseline training set consists of two million (2M) data vectors, and we also present results with enhanced sets of four (4M) and eight (8M) million training points. As our first guess on the required training size, we compute one million data vectors distributed according to

Hyper-parameter	Cosmic Shear (2x2pt)
Starting Learning Rate	5×10^{-4}
Number of Epochs	400 (600)
Batch Size	1500
ADAMW β_1	0.9
ADAMW β_2	0.999
ADAMW λ	0.01

Table 2. Hyper-parameter values we adopted when training the cosmic shear and 2x2pt emulators. We also employed the Adam minimizer with decoupled weight decay, also known as ADAMW, following Loshchilov & Hutter (2017). The parameters β_1 , β_2 and λ closely follow the nomenclature presented in Loshchilov & Hutter (2017).

a Latin Hypercube Sampling (LHS) (using package PYDOE-v0.3.6). LHS is known for its effective space-filling properties (Devon Lin & Tang 2022). However, its distribution varies based on the total number of samples. Combining two sets generated following LHS distributions results in correlated overall training data that does not have the same LHS properties. In this case, we observed a worsening of the emulator performance, so each LHS set must be generated independently. We generate all additional data vectors necessary to assemble the 2M, 4M, and 8M training sets following a uniform distribution. We could then expand the 1M initial sample to 2M, 4M, and 8M without recomputing the entire set from scratch. We did not further explore other ways of constructing data sets or other space-filling sampling methods such as the Sobol sequence (Sobol' 1967).

Given the prior knowledge of training parameters, we were able to employ both shared-memory (via OpenMP) (Dagum & Menon 1998) and message-passing (via MPI) (Forum 1994) parallelization schemes when calculating the training data vectors. We compute the data vectors at the approximate rate of 15,000 data vectors per hour per 40-core node. Our computational nodes are powered by two INTEL XEON GOLD 6148, delivering approximately 2,168 million operations per second per core². The quoted numbers illustrate that training can be accomplished in less than a day with moderate resources and computational costs of the order of a few thousand CPU hours.

Our training effectively covers the entire parameter space adopted on the growth-geometry split study Zhong et al. (2023). In this work, the cosmological parameters are restricted to a prior analogous to the one adopted by the Euclid collaboration when creating version 2.0 of the EUCLID EMULATOR for the matter power spectrum Euclid Collaboration et al. (2021). We validate the performance of all emulators using a loss function that equally weighs samples in the entire prior, being attentive in ensuring their accuracy was not position-dependent. While the EUCLID EMULATOR prior is still informative on MCMC chains containing only LSST-Y1 likelihood, the volume it encompasses is much larger than what previous emulators could simulate accurately (Boruah et al. 2023; To et al. 2023).

We implement the neural networks with PYTORCH (Paszke et al. 2019), and adopt the ADAMW as the gradient-based optimizer (Kingma & Ba 2014; Loshchilov & Hutter 2017) when training

¹ <https://github.com/CosmoLike/cocoa>

² <https://www.cpubenchmark.net/cpu.php?cpu=Intel+Xeon+Gold+6148+%40+2.40GHz&id=3176>

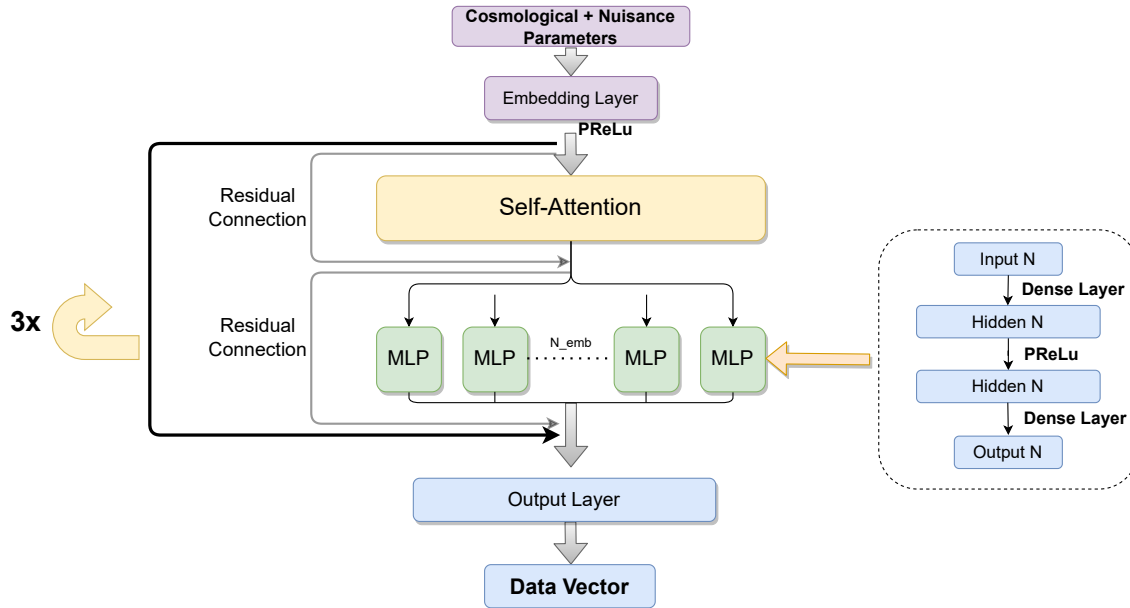


Figure 1. Proposed transformers-based neural network architecture. The input array has a dimension of 13, representing the growth-geometry split Λ CDM parameters plus the cosmic shear nuisance parameters. In the embedding layer, we employ $N_{\text{emb}} = 25$ linear transformations that take in the cosmological and nuisance parameters and produce output vectors with dimension 200. We set an activation function PReLU (He et al. 2015a) between the embedding layer and the transformer blocks. We then placed three transformer blocks. Each transformer block has a self-attention layer and N_{emb} parallel fully connected multilayer perceptrons (MLP). We employ normalization layers after the self-attention and MLP blocks (Shen et al. 2020) to ensure proper normalization of the intermediate output products. We add a residual connection (the identity operator) that adds the input vectors to the output of the self-attention block. We also added a residual connection that adds the input vector to the output of the MLP block. The MLP block, magnified in the figure above, deserves a more detailed explanation. In a few known implementations of the transformer block, the output first linear transformation is a vector with dimension \tilde{N} (drawn as *hidden N*), which differs from the input dimension N . In cases where $N \neq \tilde{N}$, there is a second linear transformation after the PReLU activation function so that the output vector also has dimension N . We tried different (\tilde{N}, N) combinations but found that $\tilde{N} = N$ offers good performance. In this case, the presence of the second linear layer is redundant, but we kept it to maintain the generality of the design. We also follow the original transformer design to keep the multiple MLPs the same within one block, this weight-sharing reduces number of trainable parameters in the architecture, which improved the accuracy in our settings. Finally, the output layer output vectors with dimension 780, correspond to the size of the cosmic shear data vector. For 2x2pt emulators, we adjusted the dimensionality of the input and output layers accordingly.

the machine learning models. Table 2 shows the starting learning rate, batch size, and number of epochs utilized in training. These values reflect our experience on what constitutes, loosely speaking, a good solution after several rounds of training and validation. Therefore, different applications may require further fine-tuning. We compare three neural network designs: a fully connected multilayer perceptron (MLP³), a 1D residual network (ResMLP⁴), and our proposed transformers-based network (TRFB) is described in Fig. 1.

We built the MLP and ResMLP emulators loosely following the prescriptions described in Boruah et al. (2023) and To et al. (2023). However, this paper should not be interpreted as providing a direct comparison between our proposed TRFB and their implementations; a comparison would require all strategies to be fully optimized. The MLP design consists of five dense layers stacked together, each of size

512. We included the PReLU activation function between the layers (Agarap 2018). The ResMLP design has a similar set of stacked layers, but we increase their size to 1024. ResMLP also contains residual connections between every two layers, which adds the original vector from the top layer to the output of the bottom one.

The training time, not counting what was needed to compute the data vectors, varied considerably depending on the pipeline design and hyper-parameter choices. Typically, it is around five hours for MLP and ResMLP models, whereas the attention-based network requires about ten hours and significantly more memory. This increased memory consumption led us to employ the high-end A100 GPU for training. Lower-tier GPUs with less memory could be used as well if, for instance, the batch size is reduced, but we have not tested how this would impact training time. We only stress that without further optimizations, Transformers is more memory-intensive than MLP and ResMLP.

We trained the cosmic shear and galaxy-galaxy lensing data vectors separately, as this increased the validation accuracy considerably. Cosmic shear and 2x2pt have similar output lengths but different input parameters; the 2x2pt has five additional nuisance parameters related to the lens’s photo- z bias and is thus more challenging to train. We did not observe additional enhancements in the final accuracy by further decomposing the data vector into smaller pieces.

³ MLP is a naming convention for feedforward neural networks with a single input and output, consisting of a stack of dense layers separated by activation functions and without recurring or residual connections.

⁴ In the literature, the term ResMLP is sometimes referred to as ResNET. Both terms can be confusing as they appear in many contexts to denote wildly different implementations of neural networks. In this work, ResMLP is used to denote a feedforward neural network with a single input and output, consisting of a stack of dense layers separated by activation functions and with residual connections connecting every two layers.

2.1.1 Emulator Input and Output

The input parameters, Θ , include both cosmological and nuisance parameters, which vary in their values by orders of magnitude and have different prior ranges $[\Theta_{i,\min}, \Theta_{i,\max}]$. We then normalize them via the redefinition

$$\theta_i = \frac{\Theta_i - \Theta_{i,\min}}{\Theta_{i,\max} - \Theta_{i,\min}}, \quad (1)$$

so all components of the vector θ are between $[0, 1]$.

We match the training set boundaries to the uniform priors displayed in Table 1, except for three modifications. First, we apply an additional cut in the directions of parameter space with Gaussian prior, limiting training points to the interval $[-3.3 \times \text{standard deviation}, +3.3 \times \text{standard deviation}]$. Second, we do not include the reionization optical depth τ as it is not a model parameter for weak lensing data vectors. Finally, we exclude shear multiplicative and galaxy linear biases since their effects can be computed with a simple multiplication as shown below (they are fast parameters in MCMC chains)

$$\begin{aligned} \xi_{\pm}^{ij}(m_i, m_j) &\rightarrow \left(\frac{1+m_i}{1+m_i^{\text{fid}}} \frac{1+m_j}{1+m_j^{\text{fid}}} \right) \xi_{\pm}^{ij}(m_i = m_i^{\text{fid}}, m_j = m_j^{\text{fid}}), \\ \gamma_t^{ij}(m_s) &\rightarrow \left(\frac{1+m_j}{1+m_j^{\text{fid}}} \right) \gamma_t^{ij}(m_j = m_j^{\text{fid}}), \\ \gamma_t^{ij}(b_i) &\rightarrow \left(\frac{b_i}{b_i^{\text{fid}}} \right) \gamma_t^{ij}(b_i = b_i^{\text{fid}}), \end{aligned} \quad (2)$$

The indexes represent redshift bins. This exclusion reduces the input dimension and simplifies the training process. For the purpose of forecasting, we use Limber approximation and do not consider redshift spatial distortion (RSD) or lensing magnification. Including these two systematics or performing the full non-Limber calculation will make the bias parameter scaling relation not linear. Another drawback of the parametrization as in Eq. 2 is that it decreases the emulator's precision whenever the fast parameters are much larger than the fiducial values even when the linear scaling relation holds. This is because the error propagates when it is being multiplied by the true $1+m_i$ or b_i . However, since we impose a stringent test for the precision of the neural network and sample fast parameters within the same order as the fiducial value, we do not expect this to be a problem. In the future, we plan to include bias parameters in the direct emulation.

Instead of directly outputting the cosmic shear or the 3x2pt data vectors, the emulator outputs a related normalized vector, denoted \mathcal{D} . To transform $\mathbf{y} \equiv \{\xi_+, \xi_-\}$ or $\{\gamma_t, w\}$ into \mathcal{D} , we first apply the change of basis

$$\bar{\mathbf{y}} = \mathbf{y}Q, \quad (3)$$

where the matrix Q contain the eigenvectors of the cosmic shear or 3x2pt covariance matrix, Σ , as shown below

$$\Sigma \equiv Q\Lambda Q^{-1}. \quad (4)$$

Here, it is possible to disregard eigenvector directions (principal components) associated with large errors; they are mostly irrelevant as the data cannot adequately constrain them. We kept all the principal components in this study for simplicity (one less parameter to be optimized). Finally, we apply the normalization

$$\mathcal{D} = \frac{\bar{\mathbf{y}} - \bar{\mathbf{y}}_{\text{mean}}}{\sigma_{\mathbf{y}}}. \quad (5)$$

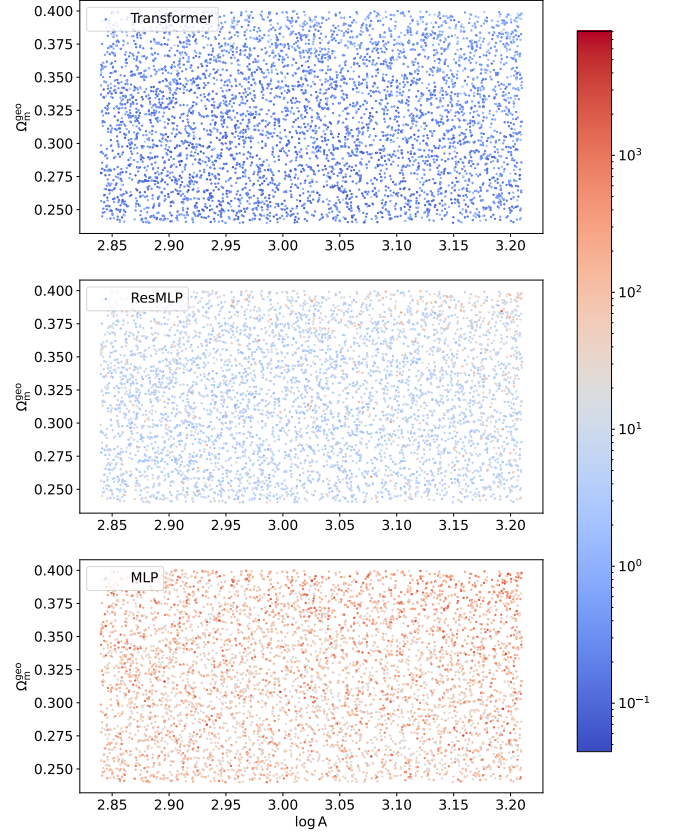


Figure 2. Projected spatial distribution of the $\Delta\chi^2$ residuals, computed on validation points, between the emulators and CoCoA, in the two-dimensional $(\Omega_m^{\text{geo}}, \log(A_s))$ plane. The figure highlights the performance difference between the transformers-based TRFB (top panel), ResNet (middle panel), and MLP (bottom panel) designs. The training was limited to the cosmic shear data vector, but it involved varying all growth-geometry Λ CDM split and nuisance parameters, except for the shear multiplicative biases. All emulators were trained with the baseline two million (2M) data vectors and tuned with the same starting learning rate, number of epochs, and batch size hyperparameters. After applying the scale cut $\theta_{\min} = \{2.756, 8.696\}$ arcmin for $\{\xi_+, \xi_-\}$, the average (median) $\Delta\chi^2$ values were 0.52 (0.30) for TRFB, 13.0 (6.1) for ResMLP, and 221.8 (76.5) for MLP. The mean and median differ by a factor of two due to significant degradation in $\Delta\chi^2$ when parameters are very close to the prior edge. For the TRFB emulator, only 10% of the validation points exhibited $\Delta\chi^2 > 1$, the adopted DES-Y3 threshold for errors to require correction via importance sampling to prevent biasing the goodness of fit.

where $\bar{\mathbf{y}}_{\text{mean}}$ is the mean of the data vectors and $\sigma_{\mathbf{y}} = \sqrt{\text{diag}[\Lambda]}$. We stored the change of basis and normalization factors alongside the neural network, enabling us to transform back to the original data vector.

2.1.2 Loss Function

We define the loss function to be the average $\Delta\chi^2$ between the data vectors computed using the neural network, \mathbf{y}_{NN} , and those calculated from CoCoA, $\mathbf{y}_{\text{CoCoA}}$. The average intentionally excludes any positional-dependent weight that could emphasize the accuracy near or far from the center of the prior volume, as shown below.

$$L(\mathbf{w}) = \left\langle (\mathbf{y}_{\text{NN}} - \mathbf{y}_{\text{CoCoA}})^T \Sigma^{-1} (\mathbf{y}_{\text{NN}} - \mathbf{y}_{\text{CoCoA}}) \right\rangle. \quad (6)$$

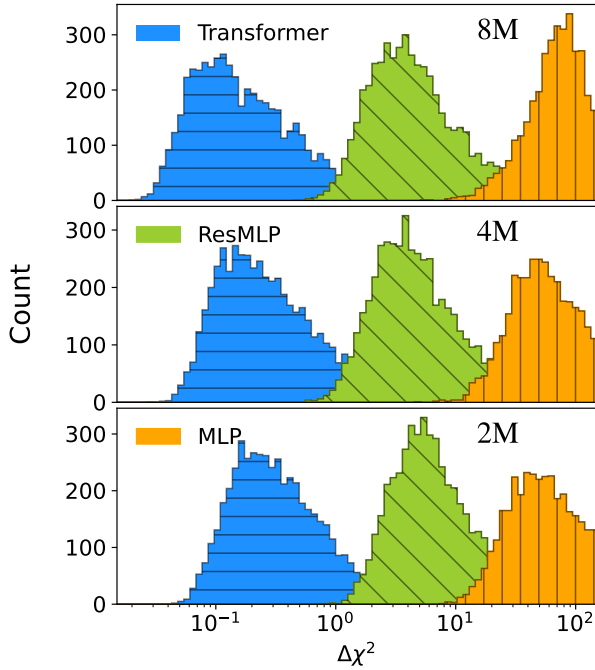


Figure 3. The cosmic shear $\Delta\chi^2$ residuals between three emulators and CoCoA, calculated on the validation set. The transformers-based TRFB emulator is shown on the blue histogram (with horizontal lines), ResMLP on the green histogram (with diagonal lines), and MLP on the orange histogram (with vertical lines). We trained all emulators with the same starting learning rate, number of epochs, and batch size hyper-parameters, detailed in Tab. 2. Although additional fine-tuning of these hyper-parameters could improve the ResMLP and MLP residuals, the enormous impact of the neural network architecture is evident. The bottom, middle, and top panels demonstrate the limited influence of increasing the size of the training set from two (2M) to eight million (8M) points. When the TRFB emulator is trained with 8M points, only 4% of the validation points have $\Delta\chi^2 > 1$, the adopted DES-Y3 threshold for errors to require corrections via importance sampling to prevent biasing the goodness of fit. Additionally, only 38.1% of the validation points exhibit residuals larger than $\Delta\chi^2 = 0.2$, the adopted DES-Y3 threshold for a model variation without refitting to be considered insignificant (Krause et al. 2021).

Here, \mathbf{w} represents the trainable weights in the machine learning design. This approach balances the emulator accuracy across the entire prior volume and guides the training to focus on the redshift and angular bins with a smaller error bar.

Furthermore, the average $\Delta\chi^2$ provides a good (but incomplete) indication of whether analyses utilizing emulators need the data likelihoods to be corrected via the Bayesian error propagation proposed in Grandón & Sellentin (2022). The drawback of this loss choice is its sensitivity to outliers; therefore, we show the entire $\Delta\chi^2$ distribution on validation points in Section 3. We left for future work investigations on alternative schemes such as the ranking and elimination of the worst few percent of points (the exact threshold to be fine-tuned) when computing the average $\Delta\chi^2$ in both training and validation.

2.1.3 Architecture

We adopt a neural network design centered on the Transformer architecture that employs the self-attention mechanism (Bahdanau et al. 2014; Vaswani et al. 2017). Transformers and its underlying self-attention have been used successfully in the construction of large

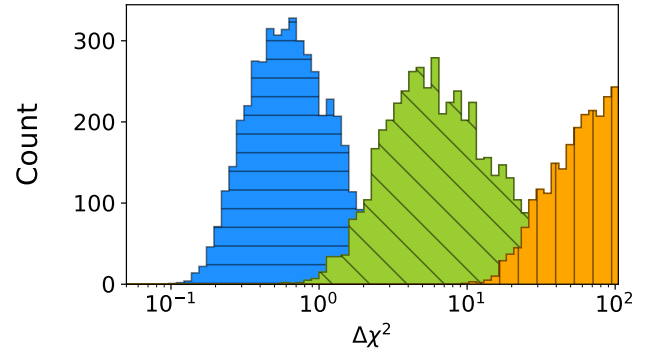


Figure 4. The 3x2pt $\Delta\chi^2$ residuals between the emulators and CoCoA, calculated on the validation set. The transformers-based emulator is shown on the blue histogram (with horizontal lines), ResMLP on the green histogram (with diagonal lines), and MLP on the orange histogram (with vertical lines). In all three cases, we independently emulated the cosmic shear and the galaxy-galaxy lensing data vectors. We trained all emulators with the same starting learning rate, number of epochs, and batch size hyper-parameters, detailed in Table. 2. We trained the 2x2pt emulators with two million points, and use the cosmic shear emulator that we have trained with eight million points.

language models with many potential applications in physics and astronomy (Bran & Schwaller 2023; Cai et al. 2023; Chen & Zhang 2023; Collado-Villaverde et al. 2023; Finke et al. 2023; Leung & Boyv 2023; Liu et al. 2023; Nan et al. 2023; Pan et al. 2023; Sui et al. 2023; Zhu et al. 2023).

The transformer architecture excels at processing sequential data, such as language and time series. Its key innovation lies in the self-attention mechanism, which calculates a weighted sum of a sequence of input vectors (Xu et al. 2015; Cheng et al. 2016). These weights are computed from mathematical operations involving three types of vectors: a query \mathbf{q} , a key \mathbf{k} , and a value \mathbf{v} . In addition, the particular operation between the query, the key, and the value vector defines different attention mechanisms. The relation between the input sequence of data and $\{Q, K, V\}$ (series of queries, keys, and values) are given by the projection matrices $\{W_Q, W_K, W_V\}$ with trainable parameters. The scaled dot-product attention is then defined via the operation:

$$\text{Attention}(Q, K, V) = \text{softmax}\left(\frac{1}{\sqrt{d_k}} QK^T\right)V, \quad (7)$$

where d_k is the dimension of the key vector. The self-attention mechanism allows the transformer model to process data more efficiently because it can capture long-range dependencies between elements of the sequence without requiring the computation of a large number of sequential operations (for instance, a long stack of dense layers). In our case, there are long-range similarities between each tomographic bin. See Tanoglidis et al. (2023) for a more in-depth review.

The complete design is illustrated in Fig. 1. The size of the total trainable parameters is about five million. The first embedding layer expands the sixteen input parameters into a set of twenty-five vectors of dimension two hundred. This process essentially maps the input data into a higher-dimensional space. These vectors serve as a richer representation of the input features, capturing complex relationships and patterns that might not be apparent in the original parameters. After the self-attention layer and the multi-head MLP layers, we applied the layer norm (Shen et al. 2020), an alternative to the conventional batch norm. Layer norm is more commonly used in transformer models (Vaswani et al. 2017), but we did not find a

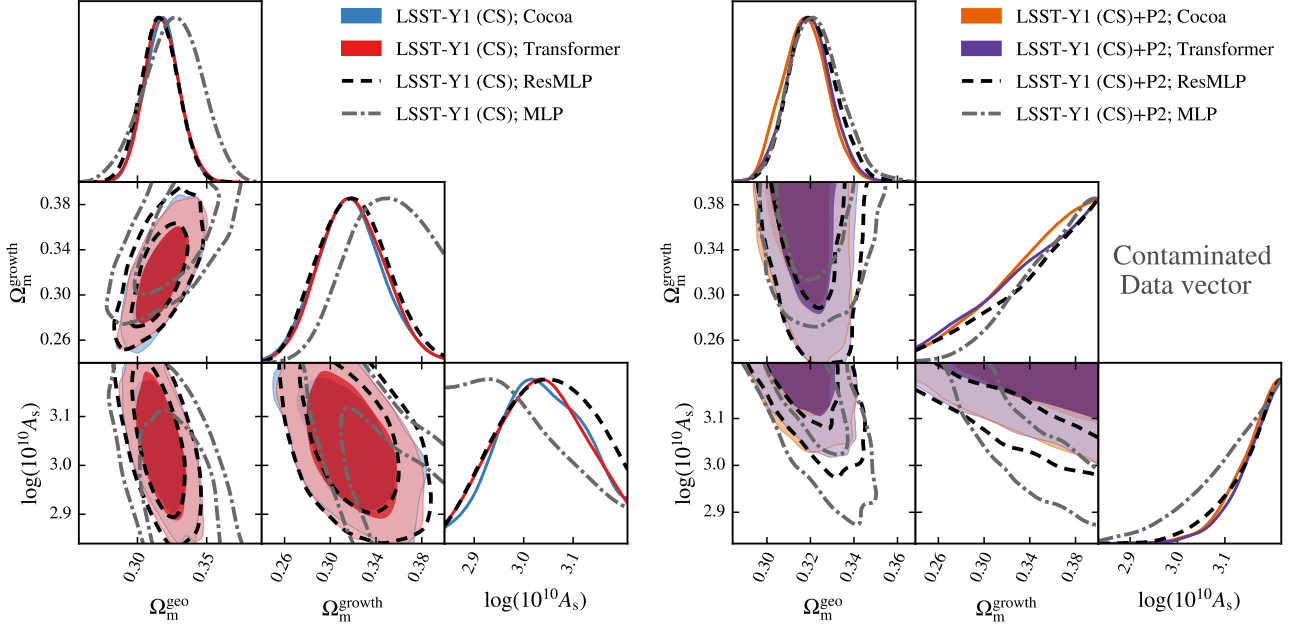


Figure 5. Posterior distributions when employing either machine learning emulators or CoCoA to compute the cosmic shear data vector. We computed the fiducial data vector adopted on all MCMC chains with CoCoA. In the left panel, the fiducial cosmology is the Λ CDM model with values displayed in Tab. 1, and the scales cut are $\theta_{\min} = 2.756, 8.696$ arcmin for $\{\xi_+, \xi_-\}$ respectively. The right panel’s fiducial model includes a dark energy component with anisotropic stresses, further elaborated in Appendix A. In this case, we made more conservative scale cuts to ensure that information from nonlinear scales is irrelevant. The exotic fiducial dark energy shifted the posterior distribution of many cosmological parameters. Compared to the left panel, this case provides a more stringent test on the consistency between the machine learning emulators and CoCoA far from the center of the prior. These chains are also illustrative of the usefulness of the growth-geometry Λ CDM split as an indicator of cracks in the validity of the smooth dark energy paradigm. Consistent with the excellent agreement we observed on $\Delta\chi^2$ tests, there is no appreciable difference in the posteriors between the transformers-based emulator and CoCoA. The ResMLP emulator also did not generate biased posteriors, but there is a visible worsening in the agreement to CoCoA. The MLP emulator exhibits the poorest performance.

difference between using the two normalization schemes. The transformer block also contains residual connections that help to reduce the so-called degradation problem (He et al. 2015b). Finally, we did not add positional embeddings into the vectors (Vaswani et al. 2017).

3 EMULATOR VALIDATION

We validate the emulators against CoCoA with five thousand random points uniformly sampled from the prior. Fig. 2 compares the TRFB, the ResMLP, and the MLP emulators on computing cosmic shear data vectors. All cosmic shear emulators are trained with two million data vectors, which we defined as the baseline scenario. We don’t introduce any noise in the data vectors, so we expect zero mean and median $\Delta\chi^2$ in the validation set for a perfectly accurate emulator. The mean (median) $\Delta\chi^2$ between the emulators and CoCoA prior to applying any scale cuts are $\langle\Delta\chi_{\text{TRFB}}^2\rangle = 0.65$ (0.38), $\langle\Delta\chi_{\text{ResMLP}}^2\rangle = 17.0$ (7.6), and $\langle\Delta\chi_{\text{MLP}}^2\rangle = 267.8$ (101.4). All panels display the $\Delta\chi^2$ after the scale cuts have been applied, and in this case $\langle\Delta\chi_{\text{TRFB}}^2\rangle = 0.52$ (0.30), $\langle\Delta\chi_{\text{ResMLP}}^2\rangle = 13.0$ (6.1) and $\langle\Delta\chi_{\text{MLP}}^2\rangle = 221.8$ (76.5).

Figure. 2 shows, for all three emulators, a uniform validation distribution of $\Delta\chi^2$ values across the two-dimensional projected $\{\Omega_m^{\text{geo}}, \log(A_s)\}$ plane. We did not detect significant $\Delta\chi^2$ spatial variations except close to the prior boundaries. This consistency is an important indication that our emulator is accurate in MCMC and nested sampling calculations regardless of the location of the fiducial data vector. Similar conclusions hold for the 3x2pt emulator.

Figure. 3 displays the $\Delta\chi^2$ validation distribution for the TRFB

(blue), ResMLP (green) and MLP (orange) designs after the cosmic shear scale cuts have been applied. The TRFB emulator improves the overall fit to the CoCoA calculations by one order of magnitude compared to ResMLP. The result is a validation distribution where only a small fraction of points has $\Delta\chi^2 > 1$, the threshold adopted by the Dark Energy Survey (DES) collaboration to indicate an error that could bias goodness-of-fit tests if not approximately corrected via Importance Sampling (Krause et al. 2021).

Figure. 3 also shows that the $\Delta\chi^2$ agreement can be slightly improved in all designs by doubling or quadrupling the points in the training set. However, even eight million (8M) data vectors do not enable the ResMLP architecture to perform better than the baseline TRFB emulator trained with two million (2M) samples. After more than one million points, the design choice for the neural network seems far more important than the training size in determining the final accuracy. This fact does not imply that more data vectors are not desirable. Training the TRFB emulator with 8M points in cosmic shear lowers the median $\Delta\chi^2$ to 0.14, below the $\Delta\chi^2 = 0.2$ threshold adopted by the Dark Energy Survey year three analysis for a model variation without refitting to be considered insignificant (Krause et al. 2021). We have not tested how far we can push the number of points to have $\Delta\chi^2 < 0.2$. However, comparing the validation distribution of the TRFB emulator trained with 2M versus 8M points suggests that learning has not yet plateaued.

Fig. 4 extends the same conclusion to the 3x2pt data vector emulation with a few modifications. First, we adopt the cosmic shear emulator with four million training points as the baseline when validating the 3x2pt data vectors. Finally, we set the 2x2pt baseline training to contain two and a half million points. These changes re-

Fiducial Cosmology										
$n_{\text{live/repeat}}$	CoCoA	TRFB 2M	TRFB 4M	TRFB 8M	ResMLP 2M	ResMLP 4M	ResMLP 8M	MLP 2M	MLP 4M	MLP 8M
1024/5d	-15.81	-15.92	-15.89	-15.85	-15.80	-15.81	-15.57	-16.73	-14.89	-16.26
	± 0.122	± 0.122	± 0.123	± 0.122	± 0.121	± 0.121	± 0.121	± 0.118	± 0.114	± 0.120
Shifted Cosmology 1										
1024/5d	-15.00	-15.14	-15.16	-14.97	-15.25	-15.21	-15.07	-15.46	-14.02	-15.33
	± 0.119	± 0.120	± 0.119	± 0.118	± 0.118	± 0.119	± 0.118	± 0.115	± 0.112	± 0.113
Shifted Cosmology 2										
1024/5d	-13.54	-13.50	-13.42	-13.53	-14.19	-13.87	-13.84	-15.33	-13.78	-14.19
	± 0.113	± 0.112	± 0.112	± 0.118	± 0.111	± 0.111	± 0.111	± 0.109	± 0.104	± 0.106

Table 3. Detailed comparison of Bayesian evidence, calculated using the POLYCHORD nested sampler with hyperparameters set at $n_{\text{live}} = 1024$, PRECISION CRITERION = 0.001, and $n_{\text{repeats}} = 5d$ in all cases. Here, d represents the number of sampled parameters. The numerical results displayed across different columns showcase the cases when we evaluate the cosmic shear data vectors using either CoCoA or the machine learning emulators (TRFB being the transformers-based design). We explored how training set sizes impact Bayesian evidence accuracy in each design, considering three scenarios: training with 2, 4, or 8 million points. We made a similar comparison with shifted data vectors, centered at $(\Omega_m, \log(A_s)) = (0.287, 3.145)$ and $(\Omega_m, \log(A_s)) = (0.25, 3.2)$, to assess the impact of prior edge effects on emulator accuracy.

duced the fraction of validation points with $\Delta\chi^2 < 1$ to be similar to what we observed when validating the baseline cosmic shear emulator (with the covariance matrix in the loss function restricted to only the cosmic shear component). We reasonably speculate from Figs. 3 and 4 that pushing the number of training points toward the twenty million range for cosmic shear and 2x2pt would drive more than half of validation points to have $\Delta\chi^2 \lesssim 0.2$.

The compatibility of the TRFB emulator with the $\Delta\chi^2 < 0.2$ requirement would allow it to be used with real data by large collaborations, including the upcoming Dark Energy Survey year six release, without the need for any additional post-processing in the MCMC chains. Emulators with this level of accuracy over such a large volume in parameter space would also facilitate the interchange of results among different collaborations. For example, the DES collaboration primarily uses the CosmoSIS framework (Zuntz et al. 2015), while the Rubin observatory Dark Energy Science Collaboration (LSST-DESC) calculates its observable using the CORE COSMOLOGY LIBRARY and FIRECROWN (Chisari et al. 2019; Prat et al. 2022). These frameworks are not easily made compatible, and combining data sets at the likelihood level with these codes is cumbersome.

We did not perform exhaustive tests to optimize the size of the training set, aiming for the least amount of points that would still respect minimum quantitative requirements involving $\langle \Delta\chi^2 \rangle$. Training all designs with the masked data vector could also reduce the required training size. We also devoted similar effort to optimizing the hyperparameters in each architecture and adjusting the number and size of each layer to avoid biases when reporting our comparison. We do not claim to have the most optimal hyperparameter solutions, and additional tuning may lower the reported $\Delta\chi^2$ even more. The emulator designs can be combined, and this is precisely what we have done in an accompanying work where we extend the emulator volume of applicability even further.

Increasing the transformer model’s complexity can reduce the size of the required training set; it can also preserve the emulator’s accuracy when training it on dark energy models with additional free parameters. For instance, we tested an enhanced version of the TRFB emulator where the embedding layer was expanded from twenty-five vectors of dimension 200 to three hundred vectors of dimension 250.

In this scenario, we found that the 2x2pt training set could be slightly reduced from two and a half to two million points while maintaining a similar fraction of points with $\Delta\chi^2 < 1$. However, the new emulator is slower to train. These settings should be adjusted according to the available computational resources.

Fig. 5 compares the posterior distributions of key cosmological parameters computed using CoCoA with those obtained from the TRFB, ResMLP and MLP emulators. On the left panel, we assumed the fiducial cosmology to be the Λ CDM model with parameters located at the center of the prior volume. We adopt the Euclid Emulator version 2.0 to compute the nonlinear matter power spectrum boost in both the Λ CDM and the growth-geometry split models (Euclid Collaboration et al. 2021). In this split cosmology, we use the growth parameters in the Euclid Emulator, following Zhong et al. (2023). In this case, Fig. 5 shows, not surprisingly, that the excellent $\Delta\chi^2$ agreement between the TRFB emulator and CoCoA translates into a good agreement at the posterior level. Fig. 5 also shows that the discrepancies at the level $\Delta\chi^2 \sim \mathcal{O}(\text{few})$ seen on the ResMLP emulator do not translate into Λ CDM parameter biases at the 68% confidence level. There are, however, noticeable differences in the $\log(A_s)$ posterior. As expected, the MLP emulator fails to reproduce accurate results.

The right panel in Fig. 5 displays the results of MCMCs in which the fiducial dark energy possesses anisotropic stresses, following the procedure detailed in Appendix A. We expanded the scale cuts, rendering information from nonlinear scales irrelevant. To find such a mask, we first set a fiducial Λ CDM cosmology and then computed the cosmic shear data vectors with (y_{NL}) and without (y_{L}) nonlinear corrections to the matter power spectrum. Then we kept eliminating scales until $\Delta\chi_{\text{L-NL}}^2 \equiv (y_{\text{NL}} - y_{\text{L}}) \mathbf{C}^{-1} (y_{\text{NL}} - y_{\text{L}})^T < 1$ at the fiducial Λ CDM model. This procedure results in the elimination of all ξ_- points and the lower limit $\theta_{\text{min}} = 30$ arcmin for ξ_+ . After the test on the fiducial model, we run an MCMC chain without any nonlinear corrections to matter power spectrum corrections. We then post-process the parameters that were accepted by the MCMC, turning on the nonlinear gravitational collapse and recomputing the LSST-Y1 likelihood. Finally, we compute the $\Delta\chi_{\text{L-NL}}^2$ distribution to visually inspect whether the scale cuts were adequate to most accepted cosmologies in the MCMC chain.

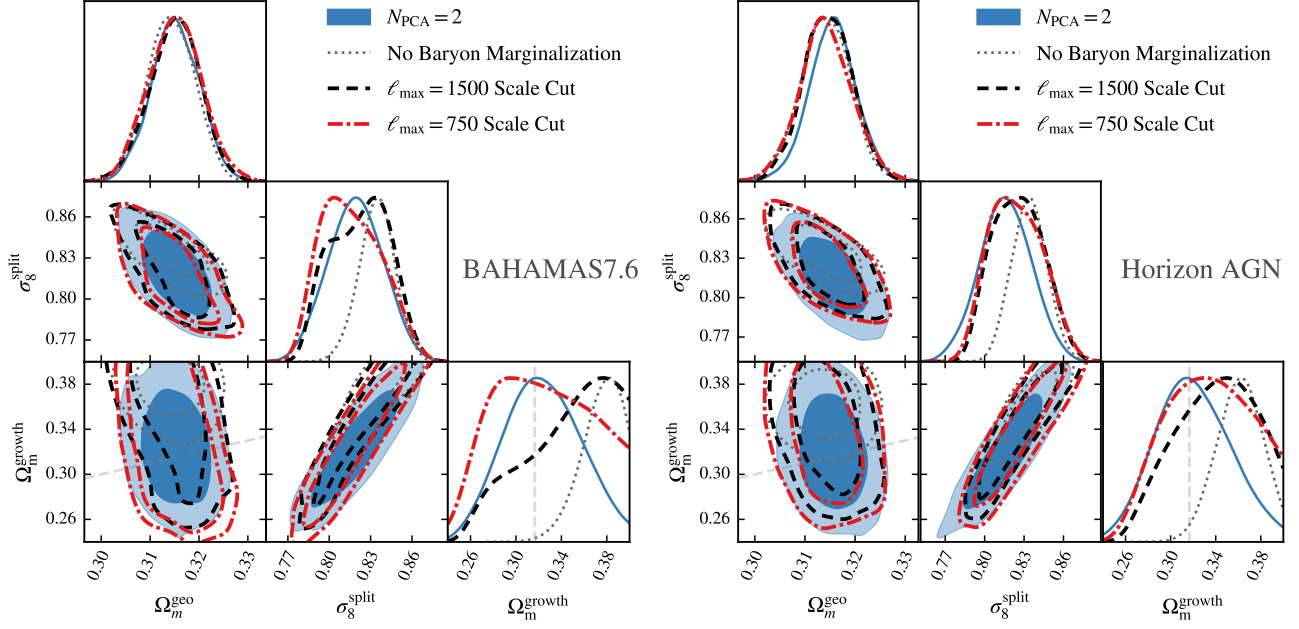


Figure 6. Posterior distributions of growth and geometry quantities in the split Λ CDM model when we introduce baryon feedback contamination on the fiducial cosmic shear data vector. The left panel assumed the feedback derived from the BAHAMAS7.6 simulation, while the right panel employed the HORIZON AGN scenario. In both panels, the gray short-dashed posteriors are the results of MCMCs in which we have not implemented any technique to mitigate baryonic effects in the theoretical computation of the data vector. On the other hand, the blue solid unbiased posteriors result from chains where we have marginalized the theoretical predictions using two principal components (see equation 11). The black-dashed and red-dot-dashed posteriors display the results from chains that assumed the more conservative scale cuts $l_{\max} = 1500$ ($\theta_{\min} = \{5.51, 17.39\}$ arcmin), and $l_{\max} = 750$ ($\theta_{\min} = \{11.02, 34.78\}$ arcmin) respectively. These angular truncations are based on the first zero-crossing of the Bessel functions that enter into ξ_+ and ξ_- calculations. In all chains, we combined the LSST-Y1 cosmic shear likelihood with the ALL external data set, which represents Planck 2018 CLIK low- ℓ EE combined with high- ℓ TTTEEE ($35 < \ell < 396$), Type Ia Supernova, BAO and BBN.

The exotic fiducial dark energy cosmology with anisotropic stresses shifts the posterior distribution of many cosmological parameters to the edge of the prior. One of the primary motivations for the growth-geometry split is to test whether the substantial disagreement between the geometric dark matter density, Ω_m^{geo} , and the growth dark matter density, Ω_m^{growth} , indicates that the underlying dark energy lies beyond the smooth dark energy paradigm (Mortonson et al. 2009). The emulators must, therefore, produce sensible results when the fiducial cosmology is far from Λ CDM. In this case, we see noticeable but not significant discrepancies between the TRFB and ResMLP emulators, with the former always being closer to CoCoA predictions.

3.1 Bayesian Evidence

The Bayesian evidence is the integral of the product of the likelihood \mathcal{L} and prior Π over the parameter space θ :

$$\mathcal{Z} = \int \mathcal{L}(\theta) \times \Pi(\theta) d\theta. \quad (8)$$

The Bayesian evidence is computationally expensive on high dimensional spaces. Evidence is ignored in Monte Carlo Markov chains, being solely a normalizing factor. However, this is a powerful tool for comparing theoretical models and the tension between different data sets (Marshall et al. 2006; Trotta 2007, 2008).

Nested Sampling (Skilling 2004) has been widely used to compute the Bayesian evidence when testing dark energy models with weak lensing and galaxy clustering data (Abbott et al. 2018a; Heymans et al. 2021; Abbott et al. 2022). This technique generates samples

within nested contours of increasing likelihood, and there are several different algorithms readily available to the community including MULTINEST (Feroz & Hobson 2008), POLYCHORD (Handley et al. 2015), DYNESTY (Speagle 2020), POCO MC (Karamanis et al. 2022), and NAUTILUS (Lange 2023).

MULTINEST and POLYCHORD have been extensively tested in the context of the Dark Energy Survey year one data (Lemos et al. 2023; Miranda et al. 2021). According to these studies, POLYCHORD produces stable results that are less sensitive to changes in the multiple hyperparameters that control their accuracy. Therefore, we adopt POLYCHORD in this work with the following conservative hyperparameters settings: $n_{\text{live}} = 1024$, PRECISION CRITERION = 0.001, and $n_{\text{repeat}} = 5d$, where d is the dimensionality of the parameter space.

The number of sampling points necessary for convergence varies between nested sampling methods, but they all seem to demand computational resources larger than what is typically required for MCMC convergence. While we are not altering the relative cost between nested samplers and Metropolis-Hasting algorithms, emulators reduce the absolute CPU expense of all statistical methods. However, Bayesian evidence computation with emulators requires them to have a large volume of reasonable accuracy. Poor or non-existent training can induce emulators to have nonsensical results due to the low-likelihood regions neglected in MCMCs (for instance, a long, flat three-sigma tail in the posterior distribution). These regions can still affect the final evidence value if they are associated with enough prior volume.

We validate the accuracy of our emulators in computing the Bayesian evidence in three distinct cosmologies, one being at the center of the cosmology prior box. We summarize the results in

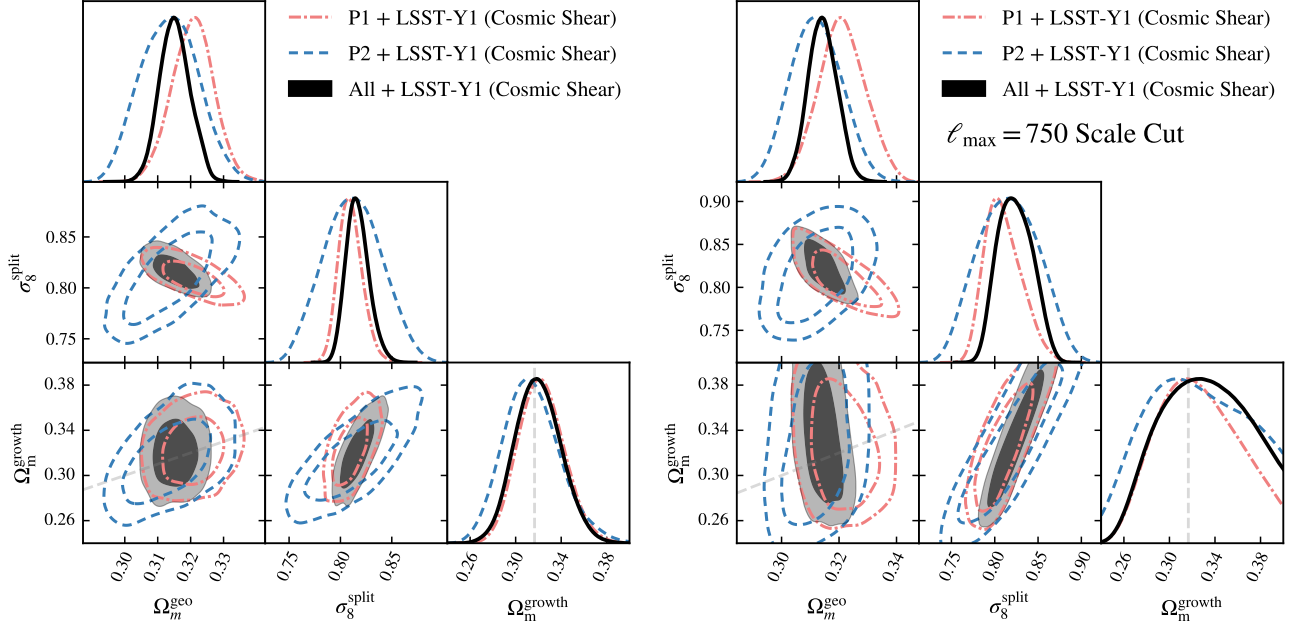


Figure 7. Posterior distributions of growth and geometry quantities in the split Λ CDM model, comparing the effects of external data sets when combined with LSST-Y1 cosmic shear. The chains in the right panel assumed the more conservative $l_{\max} = 750$ ($\theta_{\min} = \{11.02, 34.78\}$ arcmin) scale cut. These angular truncations are based on the first zero of Bessel functions that enter into ξ_+ and ξ_- calculations. The P1 external data set represents Planck 2018 CLIK low- ℓ EE combined with high- ℓ TTTEEE ($35 < \ell < 396$). The P2 data set combines Type Ia Supernova, BAO, and BBN (no information on the amplitude and tilt of scalar initial power spectrum). The ALL includes both P1 and P2. In all chains, we did not contaminate the fiducial data vector with baryonic feedback; we also assumed noiseless data vectors. The LSST-Y1 cosmic shear + ALL results, when compared against LSST-Y1 cosmic shear + P1, indicates that P2 helps testing the growth-geometry consistency by further constraining Ω_m^{geo} .

Table 3. The TRFB is the only emulator accurate within the error bars of the POLYCHORD precision. Once more, the baseline emulator trained with 2M points performs generally better than RESMLP. For RESMLP, inaccuracies become more noticeable when the posterior distribution of cosmological parameters is closer to the prior boundaries. While adding an extra few million points could, in principle, make RESMLP perform similarly to the baseline TRFB emulator on cosmic shear, we expect the comparison to be more challenging when dealing with 3x2pt data vectors. However, we leave such detailed testing for future work.

Both the computational expenditure and the execution time required to compute Bayesian evidence were a lot smaller using the TRFB emulator compared to CoCoA, by more than one order of magnitude. Such a significant difference creates new scientific opportunities, including the comparison of samplers and the reproduction of past work while spending minimal computational resources. For instance, Lemos et al. (2023) run twenty different precision settings for each N_{live} choice, while Miranda et al. (2021) runs POLYCHORD hundreds of times to calibrate the expectation value of Bayesian evidence ratios given the DES year one prior choices.

4 THE GROWTH-GEOMETRY SPLIT

The split matter power spectrum and the corresponding σ_b^{split} are defined as

$$P_{\text{split}}(k, z) = P_{\text{geo}}^{\text{linear}}(k, z) \times \left(\frac{G_{\text{growth}}^{\text{ODE}}(z)}{G_{\text{geo}}^{\text{ODE}}(z)} \right)^2 \times B^{\text{growth}}(k, z), \quad (9)$$

$$\left(\sigma_8^{\text{split}}(z) \right)^2 = \frac{1}{2\pi^2} \int d \log k W_8^2(kR) k^3 P_{\text{split}}(k, z),$$

where B^{growth} is the boost factor from the EUCLID EMULATOR v2.0 (Euclid Collaboration et al. 2021) that accounts for the non-linear contribution based on growth parameters. The linear power spectrum is rescaled according to the growth function $G(z)$ that obeys

$$G'' + \left(4 + \frac{H'}{H} \right) G' + \left[3 + \frac{H'}{H} - \frac{3}{2} \Omega_m(z) (1 - f_\nu) \right] G = 0. \quad (10)$$

Here, prime denotes the derivative with respect to the logarithm of the scale factor $\log a$, and $f_\nu = \Omega_\nu / \Omega_m$ is the fraction of the neutrino mass. The correction for neutrino mass follows the fitting formula in Kiakotou et al. (2008) to account for the relative change in the growth function, which is not included in Zhong et al. (2023). When the neutrino mass is fixed to $\sum_\nu m_\nu = 0.06$ eV, the impact of this correction is small as $f_\nu \ll 1$. In this paper, we assume the minimum neutrino mass scenario.

4.1 Forecasting Results

We adopt the TRFB emulator in all our forecasts. We combine the LSST-Y1 cosmic shear and 3x2pt simulated data with three choices

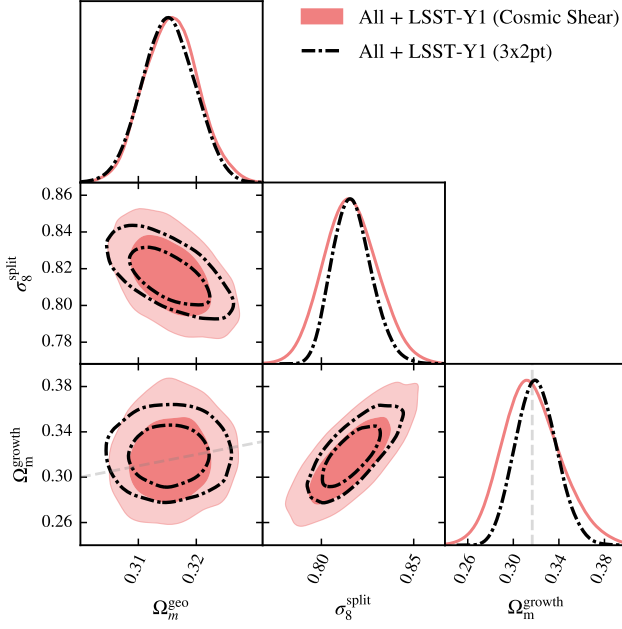


Figure 8. Posterior distributions of growth and geometry quantities in the split Λ CDM model, comparing constraints from LSST-Y1 cosmic shear and LSST-Y1 3x2pt simulated likelihoods, both combined with the ALL external data set and marginalized over baryonic effect. We found an approximately 30% improvement in the constraining of the growth parameter Ω_m^{growth} by including galaxy-galaxy lensing and galaxy clustering. In both cases, we assumed noiseless data vectors.

of external experiments that do not provide additional information on the growth parameters. The first choice, denoted P1, is a restricted version of the primary Cosmic Microwave Background Temperature and Polarization data (Zhong et al. 2023; Xu et al. 2023). P1 includes the Planck 2018 CLIK low- ℓ EE polarization likelihood combined with Planck 2018 CLIK high- ℓ TTTEEE on the restricted $35 < \ell < 396$ range (Aghanim et al. 2020). The selected multipoles prevent the gravitational lensing of the CMB from influencing the parameter posteriors. Similarly, the absence of the Planck 2018 low- ℓ TT data impedes the late-time integrated Sachs-Wolf effect from constraining the growth parameters (Hu & Sugiyama 1995; Hu et al. 1997).

The second geometry prior choice, denoted P2, comprises the combination of Type Ia Supernova data from the Pantheon sample (Scolnic et al. 2018) with baryon acoustic oscillations (BAO) and Big Bang Nucleosynthesis (BBN) constraints. The BAO data combines the SDSS DR7 main galaxy sample (Ross et al. 2015), the 6dF galaxy survey at $z_{\text{eff}} = \{0.106, 0.15\}$ (Beutler et al. 2011), and the SDSS BOSS DR12 low- z and CMASS galaxy samples at $z = \{0.38, 0.51, 0.61\}$ (Alam et al. 2017). P2 also includes the prior $100\Omega_b h^2 = 2.208 \pm 0.052$ derived from BBN Abbott et al. (2018b). Unlike P1, the P2 set provides no external information on the amplitude $\log(A_s)$ and tilt n_s of the scalar initial power spectrum. Finally, we introduce the ALL combination as a third option, which includes both P1 and P2.

The adopted fiducial scale cuts are sensitive to baryonic physics, as seen in Fig. 6. Fortunately, there are several approaches to attenuate baryonic effects on cosmic shear (Harnois-Déraps et al. 2015; Mead et al. 2021; Schneider et al. 2019; Aricò et al. 2020). Our study uses a well-established mitigation scheme based on principal components constructed from the effects that different scenarios of baryonic feed-

back imprint on the matter power spectrum at a few cosmologies; the assumption here is that these effects are not strongly correlated with cosmology (Huang et al. 2019, 2021; Eifler et al. 2014). Recent studies (Huang et al. 2021) have shown that the marginalization with respect to the leading two eigenvectors, constructed from eight different feedback scenarios, is enough to unbiased Λ CDM posteriors. Accordingly, we only added the two leading principal components, $\{\vec{e}_1, \vec{e}_2\}$, to our MCMC chains.

The principal components change the cosmic shear data vector with a linear addition that does not require our emulator to be re-trained

$$\xi_{\pm} \rightarrow \xi_{\pm} + \sum_{i=1}^2 Q_i \vec{e}_i. \quad (11)$$

We utilized eight hydrodynamical simulations to construct the principal components (eigenvectors): ILLUSTRIS TNG-100 (Springel et al. 2018), MASSIVEBLACK-II (Khandai et al. 2015), HORIZON-AGN (Dubois et al. 2014), two simulations (T8.0, T8.5) from COSMO-OWLS suite (Le Brun et al. 2014), and three simulations (T7.6, T7.8, T8.0) from the BAHAMAS suite (McCarthy et al. 2017). For the coefficients Q_i , we adopted the conservative prior $\Pi(Q_i) = \text{FLAT}[-100, 100]$.

In Fig. 6, we test the efficacy of the principal component method, restricted to two additional components, in unbiasing the cosmological parameters. We focus on the geometry and growth cold dark matter density as well as the σ_8^{split} amplitude. In the left (right) panel, we contaminated the fiducial data vector with baryonic feedback from BAHAMAS T7.6 (HORIZON AGN) simulations. Fig. 6 also compares the PCA marginalization against chains with fixed $Q_{i=1,2} = 0$, and imposed $l_{\text{max}} = 700, 1500$ cuts. The angular cuts corresponding to $l_{\text{max}} = 1500$ are $\theta_{\text{min}} = \{5.51, 17.39\}$ arcmin for $\{\xi_+, \xi_-\}$, while for $l_{\text{max}} = 700$, they are $\theta_{\text{min}} = \{11.02, 34.78\}$ arcmin (these truncations are based on the first zero of Bessel functions that enter on ξ_+ and ξ_-).

The posteriors in Fig. 6 suggest the PCA method is superior, compared to applying conservative scale-cuts, in correcting biases in the Ω_m^{growth} parameter without excessive loss of constraining power. We did not explore scales within the range $700 < l_{\text{max}} < 1500$, or further test the PCA method against simulations not used in constructing them. However, Fig. 6 reveals a sharp transition from significantly biased results with $l_{\text{max}} = 1500$ to overly-broad posterior when $l_{\text{max}} = 700$. Therefore, determining a unique l_{max} that optimizes constraints to be tighter than what PCA can accomplish while being robust against all possible scenarios may not be possible.

Fig. 7 presents Λ CDM-split forecasts, combining LSST-Y1 cosmic shear with P1, P2, or ALL external data sets. In the left panel, we maintain the fiducial scale cuts and marginalize over the parameters $Q_{i=1,2}$. The right panel employs the conservative $l_{\text{max}} = 700$ cut, with fix $Q_{i=1,2} = 0$. In all chains, we did not contaminate the fiducial data vector with baryonic feedback; we also assumed noiseless data vectors. Albeit these are consequential simplifications, Fig. 7 does show the importance of CMB data in constraining early universe parameters that do correlate with Ω_m^{growth} . The LSST-Y1 + ALL results, when compared against LSST-Y1 + P1, indicate that P2 helps testing the growth-geometry consistency by further constraining Ω_m^{geo} .

The comparison between the left and right panels in Fig. 7 reveals the large impact that small scales have in constraining Ω_m^{growth} . With the fiducial cosmic shear scale cut, the uncertainty on Ω_m^{growth} is reduced by about 53% on LSST-Y1 cosmic shear + ALL compared with the DES-Y3 cosmic shear + ALL (Zhong et al. 2023). Compared to DES-Y3 3x2pt + ALL, the uncertainty on Ω_m^{growth} is reduced

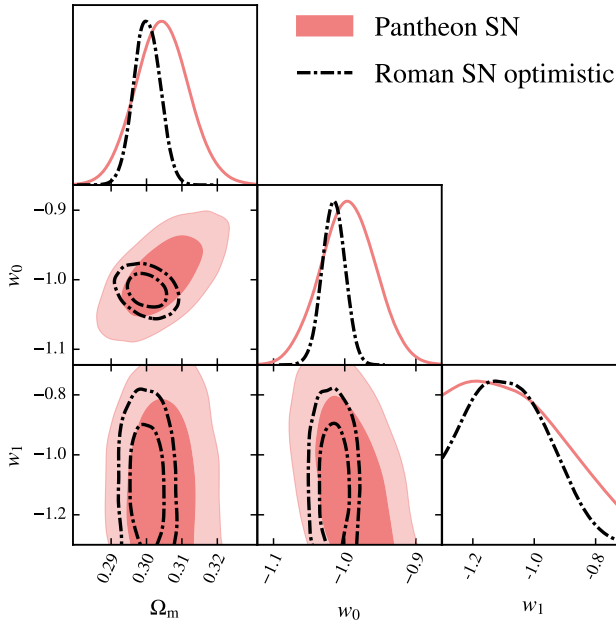


Figure 9. Posterior distributions for the late-time smooth dark energy (w_0, w_1) parameters in the two-bin model defined on equation 12. The red solid lines include Pantheon Type Ia supernova real data, while the black dot-dashed line replaces Pantheon with Roman space telescope simulated data (the optimistic IMAGING-ALLZ synthetic sample from Hounsell et al. (2018)). Both cases also include the 2018 Planck temperature and polarization data (CLIK likelihood, full multipole range) and BAO (SDSS DR7 main galaxy sample, the 6dF galaxy survey, and the SDSS BOSS DR12 low- z and CMASS galaxy samples). We utilized these posteriors to produce the growth-geometry mapping discussed in Sec. 4.2.

by about 42%. In contrast, the conservative scale cut weakens the constraining power on LSST-Y1 cosmic shear + ALL forecast to the level of DES-Y3 3x2pt + ALL. The caveat is that Zhong et al. (2023) did not explore such an aggressive scale cut for the ξ_- component. Nevertheless, our analysis demonstrates the potential improvements that are theoretically achievable with LSST-Y1 data.

Fig. 8 compares constraints on Λ CDM-split parameters derived from LSST-Y1 cosmic shear and 3x2pt, each incorporating the ALL external data set. The galaxy-galaxy lensing had simplifying assumptions; for instance, we assumed linear galaxy biases instead of higher-order and more precise prescriptions such as Hybrid Effective field theories (Kokron et al. 2021; Nicola et al. 2023). This choice prevented us from investigating the effect of more aggressive R_{\min} cuts on the split posteriors. However, this approach significantly simplified the training process for our 2x2pt machine learning emulator, as linear biases are fast parameters that only renormalize the data vector. We did not include baryonic feedback or noise in the fiducial data vector but we sampled the 2 PCs to marginalize the baryonic effect. Nonetheless, the ALL + LSST-Y1 3x2pt chain showed Ω_m^{growth} error bars that were 30% smaller compared to ALL + LSST-Y1 cosmic shear.

4.2 Limits of the Growth-Geometry Split

The main goal of the growth-geometry split is to provide a straightforward phenomenological test, without an excessive number of parameters, of the validity of the smooth paradigm for cosmic ac-

celeration (Mortonson et al. 2009). Late-time dark energy models consistent with this set of theories affect the linear growth of structures only by changing the expansion rate in eq. 10. Detection of additional scale dependency or an anomalous redshift evolution in the matter power spectrum would open new theoretical possibilities. In the growth-geometry split, the expectation is that large deviations from the smooth dark energy would trigger the split parameters to be strongly inconsistent, exemplified in the right panel of Fig. 5 as the presence of anisotropic stresses is a possible alternative to explain existing tensions outside the smooth paradigm (Koivisto & Mota 2006; Cardona et al. 2014; Majerotto et al. 2016; Garcia-Arroyo et al. 2020).

The Λ CDM split is the simplest incarnation of the growth-geometry split, as it only duplicates the cold dark matter density. Having a single additional parameter provides sensitivity to the consistency test, as both Ω_m^{geo} and Ω_m^{growth} parameters can be tightly constrained. The drawback of this simplification lies in the fact that a more general late-time dark energy equation of state can trigger $\Omega_m^{\text{geo}} \neq \Omega_m^{\text{growth}}$.

A possible strategy for testing whether detected deviations in the split parameters indicate new physics beyond smooth dark energy involves an iterative procedure. If the posterior of Λ CDM split parameters exhibit inconsistencies, then increase the number of parameters by dividing $w(z) = \text{const}$ into w^{geo} and w^{growth} components. Subsequently, if the wCDM-split consistency also fails, then increase the number of parameters again by introducing time dependency in the geometry and growth components of the dark energy equation of state. Such an iterative approach must be accompanied by Bayesian model comparison to check whether the additional parameters are justified in fitting the geometry data; otherwise, the degrading constraining power may erase the growth-geometry split usefulness (Trota 2008; Liddle 2009).

Another approach would use the most comprehensive available data to find the best, again taking into account Bayesian model comparison techniques, $w(z)$ parameterization from theoretically motivated or data-driven functional forms. Then, we split the parameters that constitute the best-fit $w(z)$, hoping the available growth data can provide sufficient constraining power for the multiple growth-related free parameters. Unfortunately, Muir et al. (2021) and Zhong et al. (2023) have indicated that there is no sufficient information in the DES 3x2pt year one and three data to constrain all growth parameters even in the wCDM split.

We propose a third solution that significantly profits from the speed enhancements our TRFB emulator offers. We advocate growth-geometry tests to be limited to the Λ CDM-split. Then, viable smooth dark energy models with more general $w(z)$ should be mapped into the $(\Omega_m^{\text{geo}}, \Omega_m^{\text{growth}})$ plane in the Λ CDM-split. As an example, we considered two time-dependent $w(z)$ parameterizations. The first model was the Chevallier, Polarski, and Linder (CPL) $w(z) = w_0 + w_a z / (1+z)$ (Chevallier & Polarski 2001; Linder 2003). The second parameterization was the piecewise equation of state defined as follows:

$$w(z) = \begin{cases} w_0, & \text{if } 0 \leq z < 1.0 \\ w_1, & \text{if } 1.0 \leq z < 2.0 \\ -1, & \text{if } z \geq 2.0. \end{cases} \quad (12)$$

The piecewise $w(z)$ provides much greater freedom in the $1.0 \leq z < 2.0$ range that current Type Ia supernova and BAO data have not been well covered; therefore, it serves well as an extreme test of the growth-geometry split.

We ran MCMC chains that assumed piecewise late-time smooth

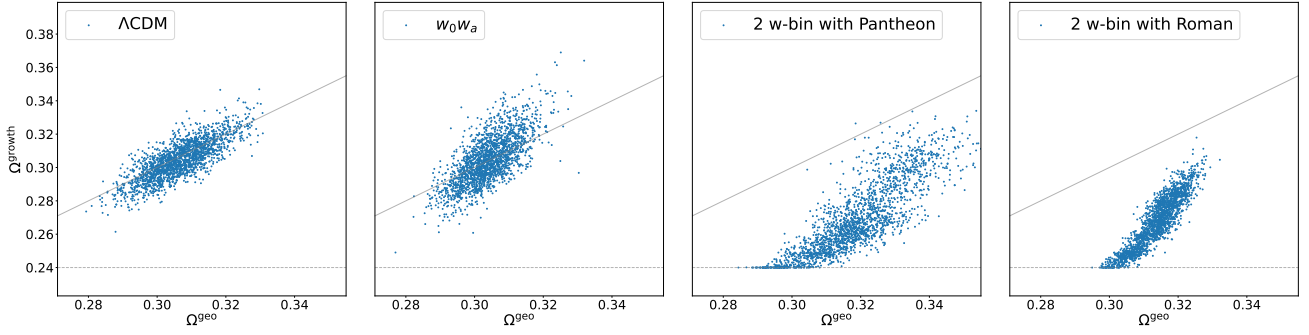


Figure 10. Best fit Ω_m^{geo} and Ω_m^{growth} parameters in the Λ CDM split when the underlying late-time dark energy model is a more general smooth dark energy model. We ran MCMC chains that assumed three illustrative $w(z)$ parameterizations: Λ (first panel), CPL (second panel) or two-parameter piecewise function (third panel). These runs constrained the cosmological parameters by combining the baseline high- ℓ TTTEEE, low- ℓ Planck power spectra, Type Ia supernova, and BAO data, following Planck Collaboration et al. (2020b). We also considered one additional chain for the piecewise $w(z)$, in which we swap the Pantheon supernova data with the optimistic IMAGING-ALLZ synthetic sample from Hounsell et al. (2018) (fourth panel). We computed the LSST-Y1 cosmic shear data vector for every accepted parameter in the MCMC chains using COSMOLIKE. For simplicity, we fixed nuisance parameters to the fiducial values displayed in Tab. 1. Finally, we minimized the LSST-Y1 likelihood to find the best Λ CDM-split parameters that approximate each model. When computing the non-linear matter power spectrum in the piecewise model, we adopted the Casarini prescription that maps the boost factor of any $w(z)$ to a w CDM model. The Λ investigation acted as a null test of our pipeline. The observed clustering of points around the $\Omega_m^{\text{geo}} = \Omega_m^{\text{growth}}$ line in the second panel is positive news as CPL encompasses what most scalar field models should predict.

dark energy. These runs constrained the cosmological parameters by combining the baseline high- ℓ TTTEEE, low- ℓ Planck power spectra, Type Ia supernova, and BAO data, following Planck Collaboration et al. (2020b). In the CPL model, we use the chains retrieved directly from the Planck Collaboration public archive⁵ (Planck Collaboration et al. 2020b). We also considered one additional chain for the piecewise $w(z)$, in which we swap the Pantheon supernova data with the optimistic IMAGING-ALLZ SN synthetic sample from Hounsell et al. (2018) that simulates the capabilities of the Roman Space Telescope. Fig. 9 compares their constraining power on w_0 and w_1 parameters, showing that Roman will be able to better probe the high redshift behavior of $w(z)$ (the rise of dark energy as explained in Linder (2021, 2023)). The IMAGING-ALLZ models the SN samples that the Roman Space Telescope could observe in the redshift range $0 < z < 3$ with only photometry, assuming the most favored scenarios on the mitigation of systematic effects.

We compute the LSST-Y1 cosmic shear data vector for every accepted parameter in the MCMC chains using COSMOLIKE. For simplicity, we fixed nuisance parameters to the fiducial values displayed in Table. 1. We can generalize this approximation in the future by assigning nuisance parameters that minimize the LSST-Y1 likelihood, which will require constructing emulators for these beyond w CDM cosmologies. When computing the non-linear matter power spectrum in the piecewise model, we adopted the Casarini prescription that maps the boost factor of any $w(z)$ to a w CDM model (Casarini et al. 2009). Finally, we minimize the LSST-Y1 likelihood to find the best Λ CDM-split parameters that approximate each model.

For the CPL $w(z)$, the second panel from the left in Fig. 10 reveals that the growth-geometry Λ CDM split does not induce an extreme $\Omega_m^{\text{geo}} \neq \Omega_m^{\text{growth}}$ incompatibility. This clustering of points around the $\Omega_m^{\text{geo}} = \Omega_m^{\text{growth}}$ line is good news because most physical scalar field models can be reasonably mapped to the CPL parameterization. However, splitting only the matter density is no longer sufficient when the background evolution is further relaxed to the more radical two-bin $w(z)$ parameterization, as shown in the third panel of Fig. 10.

The last panel in Fig. 10 shows that the additional constraining power from the Roman Space Telescope clusters the points even more. This result demonstrates the usefulness of machine learning emulators with a large volume of parameter space.

5 CONCLUSION

We built a machine-learning emulator that accurately produces, over a large volume in parameter space, the real space cosmic shear, galaxy-galaxy lensing, and galaxy clustering correlation functions for the growth-geometry split in the context of LSST-Y1. Emulators provide a realistic approach to addressing concerns on the growing computational requirements for employing current and future large-scale structure surveys in falsifying cosmological models; they can also help in the comprehensive synthetic analyses that collaborations must perform to weigh the modeling options before any data is unblinded (Krause et al. 2017, 2021).

The TRFB emulator can be seen, in some aspects, as an upgrade to the proposed machine learning-based accelerator developed in Boruah et al. (2023). Our emulator has a range of applicability in parameter volume analogous to the one adopted by the EUCLID EMULATOR v2.0. Our training method sample points using a mixture of LHS and uniform samplers, requiring a few million points for the emulator to achieve precision of the order of $\Delta\chi^2 \sim 0.2$. This number is significantly higher than the training requirement in Boruah et al. (2023), revealing that their iterative approach is still suitable. The trivial parallelization of our sampling method can reduce the required training execution time to a few hours, given enough resources.

Nonetheless, the additional complexity of our design, which contains four times more trainable parameters than the simple MLP, drove us to adopt state-of-the-art GPUs that may not be readily available everywhere, again pointing to the applicability of Boruah et al. (2023) in simple forecasting applications. The precise volume to which we can accurately train our proposed emulator depends on the number of free parameters in the dark energy model; the same is true for the required number of training points. In this regard, we have not tested how many additional parameters we can include in the

⁵ <https://www.cosmos.esa.int/web/planck>

cosmological model while maintaining the range of Λ CDM parameters to be the one given by the Euclid Emulator and still have only a small fraction of validation points with $\Delta\chi^2 > 1$. However, the relative performance of the machine-learning emulators we tested should hold regardless of the number of free parameters in the dark energy model.

We provide a detailed comparison between three machine-learning designs that illustrate the importance of adopting the state-of-the-art Transformer block when constructing emulators. Equal effort was devoted to optimizing the hyperparameters in each architecture and fine-tuning the number and sizes of layers, ensuring an unbiased comparison. We show in Fig. 3 that the TRFB emulator improves the overall fit to the CoCoA calculations by one order of magnitude compared to ResMLP and two orders of magnitude compared to MLP. Our tests reveal that increasing the transformer model's complexity can reduce the required training set at the expense of longer training times that consume way more GPU resources.

Our detailed study portrayed how different emulator designs performed when computing Bayesian evidence for cosmic shear on three fiducial cosmologies. The evidences were computed using the POLYCHORD nested sampler with conservative hyperparameters. We investigate the impact of training set sizes on Bayesian evidence accuracy for each design, considering three scenarios. The TRFB was the only emulator accurate within the error bars of the POLYCHORD precision for all training sizes and cosmologies. Nevertheless, the ResMLP did not perform poorly when trained with 8 million points. While we have not performed a similar set of comparisons for the 3x2pt emulator, fig. 4 shows an excellent $\Delta\chi^2$ agreement, taking into account the full 3x2pt covariance matrix, between TRFB and the exact calculation. Based on these findings, we anticipate that the TRFB will also be able to compute the Bayesian evidence accurately in this scenario.

As an application, the baseline TRFB emulator was employed to forecast how well the upcoming Rubin Observatory will be able to probe the consistency between Ω_m^{geo} and Ω_m^{growth} in the split Λ CDM scenario. The chosen fiducial scale cuts were sensitive to baryonic effects, as shown in Fig. 6. However, we show that principal components constructed from the effects that a few selected scenarios of baryonic feedback imprint on the matter power spectrum at a few fixed cosmologies are promising in unbiasing Ω_m^{growth} posteriors. Comparing the PC method against more conservative scale cuts on cosmic shear indicated that the former provides more constraining error bars on Ω_m^{growth} .

Fig. 7 shows forecasts on how cosmic shear can be combined with three distinct combinations of external data that do not provide information on the growth parameters. Incorporating external information on $\log(A_s)$ and n_s contributed to reducing the error bars on the growth parameter. We also compared cosmic shear against 3x2pt in Fig. 8, with the 3x2pt inference reducing Ω_m^{growth} uncertainties by approximately 30%.

Finally, Fig. 5 shows that late-time dark energy models outside the smooth paradigm of cosmic acceleration can create strong inconsistencies between Ω_m^{geo} and Ω_m^{growth} . This was observed even when the analysis was limited to cosmic shear with scales only sensitive to the linear gravitational evolution of the matter power spectrum. However, general $w(z)$ parameterizations can also yield false positives in split Λ CDM studies. Fortunately, we were able to show that viable models in the CPL $w(z)$ do not induce large variations in the difference between geometry and growth densities.

There are several avenues in which this work can be improved, including expanding the still limited volume of parameter space that the

emulator can be applied with high accuracy. The EUCLID EMULATOR parameter box is informative in statistical inferences that simulate the capabilities of the Rubin observatory. In subsequent work, we will explore alternative designs that integrate ResMLP and TRFB, as well as different training methods that will expand the volume to such an extent that the new priors will be uninformed even in the context of the Dark Energy Survey. Another improvement relates to pushing the 3x2pt toward small scales using better-motivated galaxy biases and intrinsic alignment models from an effective field theory perspective. We leave that for a future investigation.

ACKNOWLEDGEMENTS

We would like to thank Eduardo Rozo for useful discussions. The authors would also like to thank Stony Brook Research Computing and Cyberinfrastructure, and the Institute for Advanced Computational Science at Stony Brook University for access to the high-performance SeaWulf computing system, which was made possible by the National Science Foundation grant #1531492. TE is supported by the Department of Energy grant DE-SC0020215 and DE-SC0023892. EK is supported by the Department of Energy grant DE-SC0020247 and an Alfred P. Sloan Research Fellowship.

REFERENCES

- Abbott T. M. C., et al., 2018a, *Phys. Rev. D*, **98**, 043526
 Abbott T. M. C., et al., 2018b, *MNRAS*, **480**, 3879
 Abbott T. M. C., et al., 2022, *Phys. Rev. D*, **105**, 023520
 Agarap A. F., 2018, *arXiv e-prints*, p. arXiv:1803.08375
 Aghanim N., et al., 2020, *Astron. Astrophys.*, **641**, A5
 Aiola S., et al., 2020, *J. Cosmology Astropart. Phys.*, **2020**, 047
 Alam S., et al., 2017, *MNRAS*, **470**, 2617
 Alam S., et al., 2021, *Phys. Rev. D*, **103**, 083533
 Alvi S., Brinckmann T., Gerbino M., Lattanzi M., Pagano L., 2022, *JCAP*, **11**, 015
 Amon A., Efstathiou G., 2022, *MNRAS*, **516**, 5355
 Anchordoqui L. A., Barger V., Marfatia D., Soriano J. F., 2022, *Phys. Rev. D*, **105**, 103512
 Aricò G., Angulo R. E., Hernández-Monteagudo C., Contreras S., Zennaro M., Pellejero-Ibañez M., Rosas-Guevara Y., 2020, *MNRAS*, **495**, 4800
 Asgari M., et al., 2021, *A&A*, **645**, A104
 Ashoorioon A., Davari Z., 2023, *Astrophys. J.*, **959**, 120
 Bahdanau D., Cho K., Bengio Y., 2014, *arXiv e-prints*, p. arXiv:1409.0473
 Baxk T., Kurita T., Chisari N. E., Vlah Z., Schmidt F., 2023, *JCAP*, **10**, 005
 Benevento G., Kable J. A., Addison G. E., Bennett C. L., 2022, *Astrophys. J.*, **935**, 156
 Berghaus K. V., Karwal T., Miranda V., Brinckmann T., 2023
 Berryman J. M., et al., 2023, *Phys. Dark Univ.*, **42**, 101267
 Beutler F., et al., 2011, *Monthly Notices of the Royal Astronomical Society*, **416**, 3017
 Blas D., Lesgourgues J., Tram T., 2011, *J. Cosmology Astropart. Phys.*, **2011**, 034
 Boruah S. S., Eifler T., Miranda V., Krishanth P. M. S., 2023, *MNRAS*, **518**, 4818
 Bran A. M., Schwaller P., 2023, *arXiv e-prints*, p. arXiv:2310.06083
 Bridle S., King L., 2007, *New J. Phys.*, **9**, 444
 Bucko J., Giri S. K., Peters F. H., Schneider A., 2023
 Buen-Abad M. A., Chacko Z., Kilic C., Marques-Tavares G., Youn T., 2023, *JCAP*, **11**, 005
 Cai N., Han J., Jing W., Zhang Z., Zhou D., Chen X., 2023, *Research in Astronomy and Astrophysics*, **23**, 104005
 Cardona W., Hollenstein L., Kunz M., 2014, *JCAP*, **07**, 032
 Carrillo González M., Liang Q., Sakstein J., Trodden M., 2021, *JCAP*, **04**, 063

- Casarini L., Macciò A. V., Bonometto S. A., 2009, *J. Cosmology Astropart. Phys.*, 2009, 014
- Chen S.-F., Kokron N., 2023
- Chen J.-N., Zhang J.-J., 2023, *arXiv e-prints*, p. [arXiv:2311.14972](#)
- Cheng J., Dong L., Lapata M., 2016, *arXiv e-prints*, p. [arXiv:1601.06733](#)
- Chevallier M., Polarski D., 2001, *Int. J. Mod. Phys. D*, 10, 213
- Chisari N. E., et al., 2019, *Astrophys. J. Suppl.*, 242, 2
- Collado-Villaverde A., Muñoz P., Cid C., 2023, *Space Weather*, 21, e2023SW003485
- DES Collaboration et al., 2022, *arXiv e-prints*, p. [arXiv:2207.05766](#)
- DESI Collaboration et al., 2023, *arXiv e-prints*, p. [arXiv:2306.06307](#)
- Dagum L., Menon R., 1998, *Computational Science & Engineering*, IEEE, 5, 46
- Devon Lin C., Tang B., 2022, *arXiv e-prints*, p. [arXiv:2203.06334](#)
- Dore O., et al., 2019, *BAAS*, 51, 341
- Dubois Y., et al., 2014, *MNRAS*, 444, 1453
- Dutcher D., et al., 2021, *Phys. Rev. D*, 104, 022003
- Eifler T., Krause E., Schneider P., Honscheid K., 2014, *MNRAS*, 440, 1379
- Espejo J., Peirone S., Raveri M., Koyama K., Pogosian L., Silvestri A., 2019, *Phys. Rev. D*, 99, 023512
- Euclid Collaboration et al., 2021, *MNRAS*, 505, 2840
- Fang W., Hu W., Lewis A., 2008, *Phys. Rev. D*, 78, 087303
- Fang X., Eifler T., Krause E., 2020, *MNRAS*, 497, 2699
- Feroz F., Hobson M. P., 2008, *MNRAS*, 384, 449
- Finke T., Krämer M., Mück A., Tönshoff J., 2023, *Journal of High Energy Physics*, 2023, 184
- Forum M. P., 1994, Technical report, MPI: A Message-Passing Interface Standard. USA
- Franco Abellán G., Braglia M., Ballardini M., Finelli F., Poulin V., 2023, *JCAP*, 12, 017
- García-Arroyo G., Cervantes-Cota J. L., Nucamendi U., Aviles A., 2020, *Physics of the Dark Universe*, 30, 100668
- Gelman A., Rubin D. B., 1992, *Statistical Science*, 7, 457
- Gleyzes J., Langlois D., Mancarella M., Vernizzi F., 2015, *JCAP*, 08, 054
- Grandón D., Sellentin E., 2022, *arXiv e-prints*, p. [arXiv:2205.11587](#)
- Günther S., Lesgourgues J., Samaras G., Schöneberg N., Stadtmann F., Fidler C., Torrado J., 2022, *J. Cosmology Astropart. Phys.*, 2022, 035
- Hamana T., et al., 2020, *PASJ*, 72, 16
- Handley W. J., Hobson M. P., Lasenby A. N., 2015, *MNRAS*, 450, L61
- Harnois-Déraps J., van Waerbeke L., Viola M., Heymans C., 2015, *MNRAS*, 450, 1212
- He K., Zhang X., Ren S., Sun J., 2015a, *arXiv e-prints*, p. [arXiv:1502.01852](#)
- He K., Zhang X., Ren S., Sun J., 2015b, *arXiv e-prints*, p. [arXiv:1512.03385](#)
- Heymans C., et al., 2021, *A&A*, 646, A140
- Hikage C., et al., 2019, *PASJ*, 71, 43
- Hill J. C., et al., 2022, *Phys. Rev. D*, 105, 123536
- Holm E. B., Tram T., Hannestad S., 2022, *JCAP*, 08, 044
- Holm E. B., Herold L., Hannestad S., Nygaard A., Tram T., 2023, *Phys. Rev. D*, 107, L021303
- Hounsell R., et al., 2018, *ApJ*, 867, 23
- Howlett C., Lewis A., Hall A., Challinor A., 2012, *Journal of Cosmology and Astroparticle Physics*, 2012, 027
- Hu W., 2005, *Phys. Rev. D*, 71, 047301
- Hu W., 2008, *Phys. Rev. D*, 77, 103524
- Hu W., Sawicki I., 2007, *Phys. Rev. D*, 76, 104043
- Hu W., Sugiyama N., 1995, *Phys. Rev. D*, 51, 2599
- Hu W., Sugiyama N., Silk J., 1997, *Nature*, 386, 37
- Huang H.-J., Eifler T., Mandelbaum R., Dodelson S., 2019, *MNRAS*, 488, 1652
- Huang H.-J., et al., 2021, *MNRAS*, 502, 6010
- Ivezic Ž., et al., 2019, *ApJ*, 873, 111
- Karamanis M., Beutler F., Peacock J. A., Nabergoj D., Seljak U., 2022, *Monthly Notices of the Royal Astronomical Society*, 516, 1644
- Khandai N., Di Matteo T., Croft R., Wilkins S., Feng Y., Tucker E., DeGraf C., Liu M.-S., 2015, *MNRAS*, 450, 1349
- Kiakotou A., Elgaroy O., Lahav O., 2008, *Phys. Rev. D*, 77, 063005
- Kingma D. P., Ba J., 2014, *arXiv e-prints*, p. [arXiv:1412.6980](#)
- Koivisto T., Mota D. F., 2006, *Phys. Rev. D*, 73, 083502
- Kokron N., DeRose J., Chen S.-F., White M., Wechsler R. H., 2021, *Mon. Not. Roy. Astron. Soc.*, 505, 1422
- Krause E., Eifler T., 2017, *Mon. Not. Roy. Astron. Soc.*, 470, 2100
- Krause E., et al., 2017, *arXiv e-prints*, p. [arXiv:1706.09359](#)
- Krause E., et al., 2021, *arXiv e-prints*, p. [arXiv:2105.13548](#)
- Lange J. U., 2023, *Mon. Not. Roy. Astron. Soc.*, 525, 3181
- Laureijs R., et al., 2011, *arXiv e-prints*, p. [arXiv:1110.3193](#)
- Le Brun A. M. C., McCarthy I. G., Schaye J., Ponman T. J., 2014, *MNRAS*, 441, 1270
- Lemos P., et al., 2023, *MNRAS*, 521, 1184
- Leung H. W., Bovy J., 2023, *Monthly Notices of the Royal Astronomical Society*, p. stad3015
- Lewis A., Bridle S., 2002, *Phys. Rev. D*, 66, 103511
- Liddle A. R., 2009, *Ann. Rev. Nucl. Part. Sci.*, 59, 95
- Lin M.-X., Jain B., Raveri M., Baxter E. J., Chang C., Gatti M., Lee S., Muir J., 2023
- Linder E. V., 2003, *Phys. Rev. Lett.*, 90, 091301
- Linder E. V., 2021
- Linder E. V., 2023
- Liu J., Bian Y., Shen C., 2023, *arXiv e-prints*, p. [arXiv:2306.12384](#)
- Loshchilov I., Hutter F., 2017, *arXiv e-prints*, p. [arXiv:1711.05101](#)
- MacInnis A., Sehgal N., Rothermel M., 2023
- Majerotto E., Sapone D., Schäfer B. M., 2016, *Mon. Not. Roy. Astron. Soc.*, 456, 109
- Manrique-Yus A., Sellentin E., 2020, *MNRAS*, 491, 2655
- Marshall P., Rajguru N., Slosar A., 2006, *Phys. Rev. D*, 73, 067302
- McCarthy I. G., Schaye J., Bird S., Le Brun A. M. C., 2017, *MNRAS*, 465, 2936
- McCarthy F., Hill J. C., Madhavacheril M. S., 2022, *Phys. Rev. D*, 105, 023517
- McDonough E., Hill J. C., Ivanov M. M., La Posta A., Toomey M. W., 2023
- Mead A. J., Brieden S., Tröster T., Heymans C., 2021, *MNRAS*, 502, 1401
- Mergulhão T., Rubira H., Voivodic R., Abramo L. R., 2022, *JCAP*, 04, 021
- Miranda V., Rogozenski P., Krause E., 2021, *Mon. Not. Roy. Astron. Soc.*, 509, 5218
- Mortonson M. J., Hu W., Huterer D., 2009, *Phys. Rev. D*, 79, 023004
- Muir J., et al., 2021, *Phys. Rev. D*, 103, 023528
- Nan T., Cao W., Wang Z., Gao Y., Zhao L., Sun X., Na J., 2023, *Journal of Hydrology*, 625, 130085
- Nesseris S., Pantazis G., Perivolaropoulos L., 2017, *Phys. Rev. D*, 96, 023542
- Nguyen N.-M., Huterer D., Wen Y., 2023, *Phys. Rev. Lett.*, 131, 111001
- Nicola A., et al., 2020, *JCAP*, 03, 044
- Nicola A., et al., 2023
- Niedermann F., Sloth M. S., 2023
- Nygaard A., Holm E. B., Tram T., Hannestad S., 2023
- Pan J.-S., Ting Y.-S., Yu J., 2023, *arXiv e-prints*, p. [arXiv:2309.16316](#)
- Paszke A., et al., 2019, *arXiv e-prints*, p. [arXiv:1912.01703](#)
- Peirone S., Koyama K., Pogosian L., Raveri M., Silvestri A., 2018, *Phys. Rev. D*, 97, 043519
- Planck Collaboration et al., 2020a, *A&A*, 641, A1
- Planck Collaboration et al., 2020b, *A&A*, 641, A6
- Poulin V., Smith T. L., Karwal T., 2023, *Phys. Dark Univ.*, 42, 101348
- Prat J., et al., 2022, [doi:10.21105/astro.2212.09345](#)
- Raichoor A., et al., 2020, *Mon. Not. Roy. Astron. Soc.*, 500, 3254
- Ramadan O. F., Karwal T., Sakstein J., 2023
- Raveri M., Hu W., 2019, *Phys. Rev. D*, 99, 043506
- Rebouças J. a., Gordon J., de Souza D. H. F., Zhong K., Miranda V., Rosenfeld R., Eifler T., Krause E., 2023
- Ross A. J., Samushia L., Howlett C., Percival W. J., Burden A., Manera M., 2015, *Mon. Not. Roy. Astron. Soc.*, 449, 835
- Rubira H., Schmidt F., 2023
- Rubira H., Mazoun A., Garny M., 2023, *JCAP*, 01, 034
- Ruiz E. J., Huterer D., 2015a, *Phys. Rev. D*, 91, 063009
- Ruiz E. J., Huterer D., 2015b, *Phys. Rev. D*, 91, 063009
- Ruiz-Zapatero J., et al., 2021, *A&A*, 655, A11
- Sakr Z., Martinelli M., 2022, *JCAP*, 05, 030
- Schneider A., Teysier R., Stadel J., Chisari N. E., Le Brun A. M. C., Amara A., Refregier A., 2019, *J. Cosmology Astropart. Phys.*, 2019, 020

- Schöneberg N., Franco Abellán G., Pérez Sánchez A., Witte S. J., Poulin V., Lesgourgues J., 2022, *Phys. Rept.*, 984, 1
- Scolnic D. M., et al., 2018, *ApJ*, 859, 101
- Scolnic D., et al., 2022, *ApJ*, 938, 113
- Shen S., Yao Z., Gholami A., Mahoney M. W., Keutzer K., 2020, *arXiv e-prints*, p. arXiv:2003.07845
- Simon T., Franco Abellán G., Du P., Poulin V., Tsai Y., 2022, *Phys. Rev. D*, 106, 023516
- Skilling J., 2004, in Fischer R., Preuss R., Toussaint U. V., eds, American Institute of Physics Conference Series Vol. 735, Bayesian Inference and Maximum Entropy Methods in Science and Engineering: 24th International Workshop on Bayesian Inference and Maximum Entropy Methods in Science and Engineering. pp 395–405, doi:10.1063/1.1835238
- Sobol' I., 1967, *USSR Computational Mathematics and Mathematical Physics*, 7, 86
- Speagle J. S., 2020, *MNRAS*, 493, 3132
- Springel V., et al., 2018, *MNRAS*, 475, 676
- Spurio Mancini A., et al., 2019, *MNRAS*, 490, 2155
- Spurio Mancini A., Piras D., Alsing J., Joachimi B., Hobson M. P., 2022, *MNRAS*, 511, 1771
- Sui J., Tian Y., Li Y., Wu N., 2023, *Geophysics*, 88, WC107
- Tanoglidis D., Jain B., Qu H., 2023, *arXiv e-prints*, p. arXiv:2310.12069
- The LSST Dark Energy Science Collaboration et al., 2018, *arXiv e-prints*, p. arXiv:1809.01669
- To C.-H., Rozo E., Krause E., Wu H.-Y., Wechsler R. H., Salcedo A. N., 2023, *J. Cosmology Astropart. Phys.*, 2023, 016
- Torrado J., Lewis A., 2021, *JCAP*, 05, 057
- Trotta R., 2007, *Mon. Not. Roy. Astron. Soc.*, 378, 819
- Trotta R., 2008, *Contemp. Phys.*, 49, 71
- Vaswani A., Shazeer N., Parmar N., Uszkoreit J., Jones L., Gomez A. N., Kaiser L., Polosukhin I., 2017, *arXiv e-prints*, p. arXiv:1706.03762
- Wang S., Hui L., May M., Haiman Z., 2007, *Phys. Rev. D*, 76, 063503
- Wang Z., Mirpoorian S. H., Pogossian L., Silvestri A., Zhao G.-B., 2023, *JCAP*, 08, 038
- Xu K., Ba J., Kiros R., Cho K., Courville A., Salakhutdinov R., Zemel R., Bengio Y., 2015, *arXiv e-prints*, p. arXiv:1502.03044
- Xu J., et al., 2023
- Zhao C., et al., 2022, *MNRAS*, 511, 5492
- Zhong K., Saraivanov E., Miranda V., Xu J., Eifler T., Krause E., 2023, *Phys. Rev. D*, 107, 123529
- Zhu R., et al., 2023, *Frontiers in Physics*, 11, 1266927
- Zumalacárregui M., Bellini E., Sawicki I., Lesgourgues J., Ferreira P. G., 2017, *JCAP*, 08, 019
- Zuntz J., et al., 2015, *Astronomy and Computing*, 12, 45

APPENDIX A: NON-SMOOTH DARK ENERGY INJECTION

This Appendix describes how we generated LSST-Y1 data vectors with non-smooth dark energy that contained anisotropic stresses. We employed the Parameterized Post-Friedmann Framework (PPF) (Hu & Sawicki 2007; Fang et al. 2008; Hu 2008) because the fluid description suffers from singularities when the dark energy equation of state crosses $w = -1$. The PPF parameterization replaces the fluid equation, and thus avoid the singularities, by establishing a direct correspondence between dark energy fluid and dark matter in the large-scale limit. It also introduces an effective sound speed c_Γ to describe perturbations in the small scale limit. PPF introduces a form for interpolating the large and small scale limit (Hu 2005):

$$\lim_{k_H \ll 1} \Gamma' = S - \Gamma. \quad (\text{A1})$$

Here, $k_H = k/aH$ and the source term is

$$S = \frac{g' - 2g}{g+1} \frac{\Phi - \Psi}{2} - \frac{4\pi G}{(g+1)k_H^2 H^2} \left\{ g \left[(\rho_T \pi_T)' + \rho_T \pi_T \right] - \left[(g + f_\zeta + g f_\zeta) (\rho_T + p_T) - (\rho_e + p_e) \right] k_H V_T \right\}. \quad (\text{A2})$$

In this description, the subscript T stands for other components: matter, radiation, and neutrinos.

The function Γ is related to the rest frame dark energy density perturbation via the Poisson equation:

$$k^2 \Gamma = -4\pi G a^2 \delta \rho_{\text{DE}}^{\text{rest}}. \quad (\text{A3})$$

The free functions in PPF is reduced to a scale and time-dependent metric fluctuation $g(\ln a, k)$ and a time-only-dependent function $f_\zeta(a)$. Note that they can be mapped to specific modified gravity models such as $f(R)$ or DRP (Hu & Sawicki 2007). We follow the phenomenological parameterization (Hu 2008):

$$g(\ln a, k) = g_0 \left(\frac{\rho_e}{\rho_T} \frac{\Omega_T}{\Omega_e} \right)^{1/2} \left(1 + (c_g k_H)^2 \right)^{-1}. \quad (\text{A4})$$

and

$$f_\zeta(a)(\ln a) = 0.4 g_0 \left(\frac{\rho_e}{\rho_T} \frac{\Omega_T}{\Omega_e} \right)^{1/2}. \quad (\text{A5})$$

Previous studies have found, using the full shape Planck 2015 CMB temperature and polarization data, constraints on g_0 centered at zero (no anisotropic stress) with a standard deviation $\sigma_{g_0} \approx 0.2$ (García-Arroyo et al. 2020). For this study, we chose an extreme case $(g_0, c_g) = (-1, 0.01)$ to exemplify the impact of such models on the Λ CDM growth-geometry split parameters. Finally, we replace the matter power spectrum with the Weyl potential auto spectrum on cosmic shear (DES Collaboration et al. 2022; Spurio Mancini et al. 2019).

This paper has been typeset from a $\text{\TeX}/\text{\LaTeX}$ file prepared by the author.